Combining an optimisation-based frequency band identification method with historical data for novelty detection under time-varying operating conditions

Stephan Schmidt[a,*], Konstantinos C. Gryllias[b,c]

[a] *Centre for Asset Integrity Management, Department of Mechanical and Aeronautical Engineering, University of Pretoria, Pretoria, South Africa*
[b] *Department of Mechanical Engineering, KU Leuven, Celestijnenlaan 300, 3001 Heverlee, Belgium*
[c] *Dynamics of Mechanical and Mechatronic Systems, Flanders Make, Belgium*

Abstract

Incipient damage detection is important for critical rotating machines such as gearboxes found in the power generation, mining and aeronautical industries. However, the fault information frequently manifests in weak frequency bands in the vibration signals and the fault diagnosis process is impeded by time-varying operating conditions. Frequency band identification methods can be used to enhance the weak fault information in the vibration signal, however, this process is impeded by impulsive components unrelated to the component-of-interest and time-varying operating conditions. Hence, in this work, an optimisation-based frequency band identification method is developed to address these shortcomings. This method comprises of two steps; in the first step, a coarse informative frequency band procedure is used, whereafter a derivative-free optimisation algorithm is utilised to find the optimal frequency band for fault diagnosis. Since many rotating machines operate for long periods of time in a healthy condition, much healthy historical data are usually available when continuous monitoring is performed. Hence, this historical data are used with the proposed frequency band identification approach for automatic fault detection. The method is investigated on two experimental datasets acquired under time-varying operating conditions and compared to other existing approaches for fault diagnosis. The results indicate that the method is very capable of enhancing the fault information and can be used for automatic fault detection under time-varying operating conditions.

Keywords:

Diagnostics, Frequency Band Identification, Optimisation, Time-varying operating conditions, Historical data, Gearboxes

*Corresponding author.
Email address: stephan.schmidt@up.ac.za (Stephan Schmidt)

1. Introduction

Damaged rotating machines such as gearboxes could result in unexpected failures of expensive critical assets such as wind turbines [1, 2]. The damage could manifest such as changes in the machine's response signature or the machine's performance and can be detected with the appropriate condition monitoring measurements [3]. The condition of rotating machines such as gearboxes and motors can for example be inferred from vibration measurements [2], acoustic measurements [4–7], current measurements [8, 9], oil debris monitoring [3] and temperature measurements [3, 10, 11]. Temperature measurements are not as effective as other methods for incipient damage detection; and even though oil debris monitoring is much more sensitive to damage, it is usually performed by taking periodic samples from the data [3]. Acoustic emission measurements could offer early fault detection, but its performance is impeded by difficulties in signal processing, it is sensitive to background noise, and it is sensitive to the transmission path [6]. In Ref. [6], the performance of acoustic emission was improved by placing the sensor inside the gearbox casing and it showed much earlier signs of damage when compared to vibration measurements.

Vibration-based condition monitoring methods are widely used for gearbox condition monitoring and is considered the most common condition monitoring method for rotating machines [3]. This is because the measured vibration signals contain much information related to the instantaneous condition of the machine and it has relatively low costs involved with their implementation [3, 12]. However, it can be difficult to observe the fault signatures associated with the damaged components, because they can be masked by time-varying operating conditions [12–14], impulsive noise [15, 16] and dominant deterministic phenomena such as gear mesh interactions [17].

Impulses generated by the damaged components often excite the structural time-invariant resonances, which results in the diagnostic information to manifest in narrow frequency bands [18, 19]. It is possible to increase the signal-to-noise ratio of the components-of-interest by amplifying these frequency bands. This is one of the motivations behind using the spectral kurtosis and the kurtogram for fault diagnosis applications [20]. The kurtogram is used to automatically identify the frequency band that maximises the kurtosis, which can subsequently be used to design a bandpass filter to automatically extract this component [21]. Even though the kurtogram has been successful for bearing [21] and gear diagnostics [19], it cannot distinguish between a single transient and repetitive transients and the original kurtogram used a spectrogram-based estimator. This could lead to the wrong or suboptimal frequency band to be identified [22]. Hence, various other methods such as the protrugram [23], the improved kurtogram [24], the optimised spectral kurtosis [25], the infogram [22], and the envelope harmonic-to-noise ratio [26] have been proposed as alternatives to the original kurtogram. Hebda-Sobkowicz et al. [16] performed a comparison of different frequency band identification methods under non-Gaussian noise conditions.

The aforementioned techniques do not require any prior knowledge about the kinematics of the machine and are therefore referred to as blind methods [27]. It is possible to incorporate prior knowledge about the kinematics of the machine to determine frequency bands that are optimal to identify specific components (e.g. the Ball-Pass Order of the Outer race (BPOO) component of a bearing). These methods are referred to as targeted methods [27]. Smith et al. [27] compared different frequency band identification methods for fault diagnosis and found that targeted methods perform better than blind methods. Mauricio et al. [28] developed the IESFOgram to automatically determine the optimal frequency band for calculating the Improved Envelope Spectrum (IES), which has been very successful for bearing fault diagnosis. Schmidt et al. [29] proposed the IFBI_{α}gram, which uses a targeted signal-to-noise ratio feature for bearing and gear fault diagnosis. The distcsgram is another targeted method that uses an indicator developed for identifying frequency bands that contain much evidence that the bandlimited signal is generalised Gaussian cyclostationary rather than generalised Gaussian stationary [30].

Historical data can be also be combined with the frequency band identification to find informative frequency bands or to enhance the fault information. Wang et al. [31] proposed the SKRgram which selects the frequency band with the largest increase in kurtosis when compared to a reference signal. Schmidt et al. [18] developed a methodology that enhances the novel information in frequency bands by combining empirical models with frequency band identification approaches. Liu et al. [32] developed the accugram; a frequency band identification method that uses the classification accuracy as a metric.

The aforementioned frequency band identification methods are usually estimated with the Short-Time Fourier Transform (STFT) or the Wavelet Packet Transform (WPT) estimators [21, 27] and therefore the resulting feature planes have fixed resolutions. Hence, Zhang and Randall [33] used genetic algorithms to refine the frequency band that was identified with the kurtogram to improve its performance. Wang et al. [34] proposed a ratio of harmonics of the defect component-to-residual component measure and combined it with a genetic algorithm to find the optimal frequency band. Blind deconvolution methods use an estimated deconvolution filter to extract the impulsive or cyclostationary information from the signals [35].

However, many rotating machines operate inherently under time-varying operating conditions (e.g. wind turbines) and could adversely influence the application of the conventional frequency band identification methods. Only few methods have made a systematic attempt to solve the frequency band identification problem under time-varying operating conditions (e.g. [18, 28, 29]). In addition to this, the cyclic spectrum of the spectrogram is biased [17], which could adversely influence the results if targeted frequency band identification methods are used. Lastly, rotating machines operate in healthy conditions for long periods, which makes healthy data easily available when continuous condition monitoring is per-

formed. This information can be used to perform automatic novelty detection using the frequency band identification methods. The authors are not aware of any methods combining healthy historical data with frequency band identification methods for novelty detection. We therefore propose a method to find the optimal informative frequency band under time-varying operating conditions and combine this with historical data from a healthy machine to perform novelty detection. The performance of this method is demonstrated on experimental datasets that were acquired under time-varying operating conditions. The contributions of this work are summarised here:

- A new framework is proposed that finds the optimal frequency band to enhance the fault information in a vibration signal in two-steps, namely, an initialisation step and an optimisation step. The method is developed for blind and targeted features.
- The method is specifically developed for applications under time-varying operating conditions.
- A novelty detection procedure is proposed that combined with frequency band identification methods under time-varying operating conditions.

The layout of the paper is as follows: In Section 2, the proposed method is presented, whereafter it is critically applied and evaluated in Section 3 on two experimental datasets. Existing methods are applied on the experimental data in Section 4 to highlight the performance of the proposed method. Finally, the paper is concluded in Section 5 with recommendations also made for future work. Three appendices are included with additional information; Appendix A contains information pertaining to the optimisation algorithm used in this work; Appendix B contains the results obtained with the raw experimental signals; and Appendix C investigates the influence of the initialisation parameters.

2. Proposed method

We desire to extract a bandlimited signal $\boldsymbol{x_f}$ from the measured vibration signal $\boldsymbol{x} \in \mathbb{R}^{N_x}$ with a bandpass filter $\boldsymbol{h_f}$ that has a passband $\boldsymbol{f} = [f_l, f_h]$. The resulting filtered signal

$$\boldsymbol{x_f} = \boldsymbol{h_f} \otimes \boldsymbol{x}, \tag{1}$$

$$= [x[0; f_l, f_h], x[1; f_l, f_h], \ldots, x[N_x - 1; f_l, f_h]]^T, \tag{2}$$

can then subsequently be used in combination with signal analysis methods (e.g. synchronous average, squared envelope spectrum, improved envelope spectrum [18, 22, 23]) for fault diagnosis. We can formulate

the informative frequency band identification problem as

$$\underset{\boldsymbol{f}}{\text{maximise}} \quad \Psi(\boldsymbol{f};\boldsymbol{x}) \tag{3}$$

$$\text{subjected to} \quad \Delta f_{min} - f_l \leq 0 \tag{4}$$

$$f_h - \frac{f_s}{2} + \Delta f_{max} \leq 0 \tag{5}$$

$$\Delta f_{lh} + f_l - f_h \leq 0, \tag{6}$$

with the value for $\min\{f_l\} = \Delta f_{min}$, the value for $\max\{f_h\} = f_s/2 - \Delta f_{max}$, the minimum allowable bandwidth of the bandpass filter $\min\{f_h - f_l\} = \Delta f_{lh}$ and the score assigned to the frequency band $\boldsymbol{f}$ for the signal $\boldsymbol{x}$ is denoted $\Psi(\boldsymbol{f};\boldsymbol{x}) : \mathbb{R}^2 \to \mathbb{R}$. This score function, which aims to quantify the amount of fault information in the frequency band $\boldsymbol{f}$, can be blind (e.g. kurtosis) or targeted (e.g. an indicator-of-cyclostationarity) and can be calculated from the raw signal; the cyclic spectrum of the signal or from the order-frequency spectral coherence of the signal. Since the bandpass filter has roll-off effects and it is not expected that the informative frequency band will be close to 0 Hz or close to the Nyquist frequency $f_s/2$, $\Delta f_{min} = 50$ Hz and $\Delta f_{max} = 50$ Hz is used in this work. The minimum bandwidth Δf_{lh} was set equal to 20 Hz, since it is suggested in Refs. [23, 25] that the passband should contain at least three harmonics of the fault component.

The optimisation problem in Equations (3) - (6) can easily be written in an equivalent unconstrained minimisation form

$$\underset{\boldsymbol{f}}{\text{maximise}}\ \kappa(\boldsymbol{f}), \tag{7}$$

by using the penalty method [36], where

$$\kappa(\boldsymbol{f}) = \Psi(\boldsymbol{f};\boldsymbol{x}) - r \cdot \left(\max\left\{\Delta f_{min} - f_l, 0\right\}^2 + \max\left\{f_h - f_s/2 + \Delta f_{max}, 0\right\}^2 + \max\left\{\Delta f_{lh} + f_l - f_h, 0\right\}^2 \right), \tag{8}$$

is the unconstrained objective function that needs to be maximised. In Equation (8), $r \in \mathbb{R}^+$ is a penalty parameter and $\max\{a, b\}$ returns the largest number between a and b. Unconstrained minimisation solvers [37, 38] can be used if the objective function is written as $-\kappa(\boldsymbol{f})$. The r in this work is set equal to 10^9.

The proposed method to find the optimal frequency band $\boldsymbol{f}$ using a score function $\Psi(\boldsymbol{f};\boldsymbol{x})$ and the unconstrained objective function in Equation (8) is summarised in Figure 1. The optimal passband $\boldsymbol{f} = [f_l, f_h]$ is determined in two steps for a vibration signal $\boldsymbol{x}$ acquired from a machine in an unknown condition, namely, the initialisation procedure and the optimisation procedure. The initialisation procedure, discussed in Section 2.2, is guided by the cost function in Equation (8) to determine a good initial value for the centre of the bandpass filter $f_c = (f_l + f_h)/2$. The optimisation procedure, discussed in

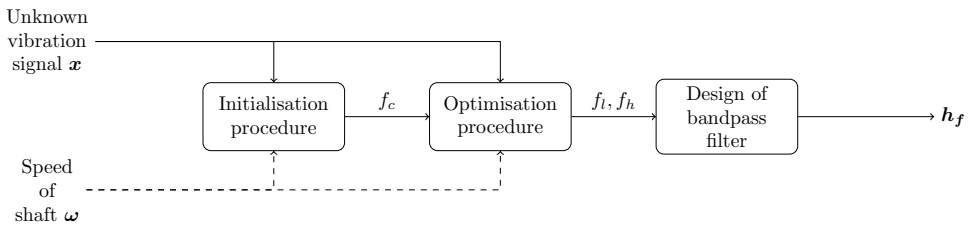

Figure 1: The proposed procedure to find an optimal bandpass filter $\boldsymbol{h}_f$, with a passband $\boldsymbol{f} = [f_l, f_h]$, that will enhance the potential fault information in a vibration signal $\boldsymbol{x}$ acquired from a unknown condition. This is performed with a preselected scoring function $\Psi(\boldsymbol{f}; \boldsymbol{x})$. The rotational speed of the shaft, denoted $\boldsymbol{\omega}$, is only necessary for targeted scoring functions and therefore indicated by a dashed line.

Section 2.3, determines the passband $\boldsymbol{f} = [f_l, f_h]$ that maximises the cost function in Equation (8). The optimal passband is used to find the impulse response function of the bandpass filter $\boldsymbol{h_f}$. Thereafter, the filtered signal $\boldsymbol{x}_f = \boldsymbol{h_f} \otimes \boldsymbol{x}$ is analysed for damage.

Only some scoring functions $\Psi(\boldsymbol{f}; \boldsymbol{x})$ require the rotational speed $\boldsymbol{\omega}$ information and therefore this is not always necessary as highlighted by the dashed line in Figure 1. More information on the different kinds of score functions is given in Section 2.1.

2.1. Score function

It is desired to identify a frequency band that is optimal for fault diagnosis and therefore it is important to utilise a scoring function that quantifies the amount of fault information in a frequency band $\boldsymbol{f}$. The calculation procedure of blind and targeted features is different under time-varying operating conditions. The calculation of the objective function $\Psi(\boldsymbol{f}; \boldsymbol{x})$ associated with a blind feature is shown in Figure 2. If

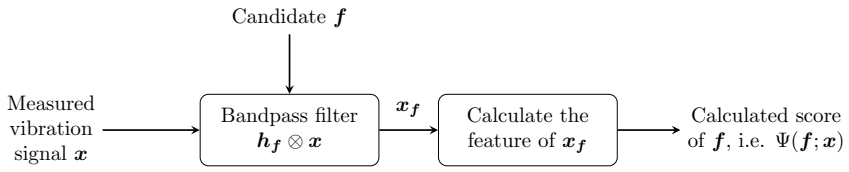

Figure 2: The calculation of the score $\Psi(\boldsymbol{f}; \boldsymbol{x})$ is shown for the case where the feature is blind, e.g. kurtosis [21] or spectral negentropy [22].

a targeted objective function is used, where the cyclic orders $\boldsymbol{\alpha}$ are targeted, then the objective function $\Psi(\boldsymbol{f}; \boldsymbol{x}, \boldsymbol{\omega}, \boldsymbol{\alpha})$ needs to be calculated as shown in Figure 3. It is important to perform order tracking to

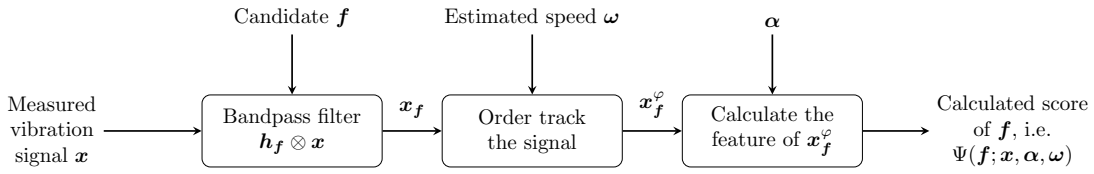

Figure 3: The calculation of the score $\Psi(\boldsymbol{f}; \boldsymbol{x}, \boldsymbol{\omega}, \boldsymbol{\alpha})$ is shown for the case where the feature (e.g. ICS2 [27]) is targeted on the cyclic orders $\boldsymbol{\alpha}$. The order tracked signal is denoted by the superscript φ, i.e. $\boldsymbol{x}^\varphi$.

ensure that the features have a consistent representation under time-varying speed conditions and therefore

the rotational speed $\boldsymbol{\omega}$ (or instantaneous phase) of the shaft is required as an input. If the rotational speed is available, computed order tracking is performed. In computed order tracking, the signal is resampled by using the phase information from the reference shaft. A detailed overview of computed order tracking given in Ref. [39]. If the speed cannot be measured, it is possible to use tacholess order tracking methods to perform this task [40, 41]. In Figure 3, order tracking is performed after the filtering process to ensure that the angle-time cyclostationary characteristics of the impulses are retained [42]. However, performing order tracking in each function evaluation increases the computational cost of the optimisation procedure and therefore if the gearbox is operating under constant or quasi-stationary conditions, the order tracking can be neglected to improve the computational time required for the function evaluations.

The focus of this paper is placed on a signal-to-noise metric that was used in Ref. [18] to estimate the prominence of the cyclic orders $\boldsymbol{\alpha}$ in the SES of a filtered vibration signal. This metric was slightly adapted and used as an integral step in the IFBI$_\alpha$gram [29], which is a targeted frequency band identification method. The feature

$$\Psi_{prom}(\boldsymbol{f};\boldsymbol{x},\boldsymbol{\alpha},\boldsymbol{\omega}) = \sum_{\alpha\in\boldsymbol{\alpha}} \frac{\mathrm{SES}_{\boldsymbol{x}_{\boldsymbol{f}}^{\varphi}}(\alpha)}{\mathrm{noise}\left\{\mathrm{SES}_{\boldsymbol{x}_{\boldsymbol{f}}^{\varphi}}(\alpha)\right\}}, \tag{9}$$

aims to extract the prominence of the cyclic order components $\boldsymbol{\alpha}$ in the signal. The Squared Envelope Spectrum (SES) of the bandlimited signal $\boldsymbol{x}_{\boldsymbol{f}}^{\varphi}$ is denoted by $\mathrm{SES}_{\boldsymbol{x}_{\boldsymbol{f}}^{\varphi}}(\alpha)$ in Equation (9). The SES of the signal $\boldsymbol{x}\in\mathbb{R}^{N_x}$ is calculated with

$$\mathrm{SES}_{\boldsymbol{x}}(\alpha) = \left| \frac{1}{N_x} \sum_{n=0}^{N_x-1} |x[n]|^2 \, e^{-j2\pi n\alpha/f_s} \right|. \tag{10}$$

The Squared Envelope Spectrum (SES) highlights the cyclostationary content in the instantaneous power of a signal and is a very popular technique for bearing diagnostics [17, 18]. This feature calculated with Equation (9) is maximised when the signal components associated with the targeted cyclic orders $\boldsymbol{\alpha}$ are very prominent (i.e. have high signal-to-noise ratios) in the SES. Hence, this feature indicates in which frequency bands it would be easy to identify the cyclic components associated with the damaged component-of-interest.

However, the analytical cyclic orders may differ from the actual cyclic orders of the component-of-interest due to slip or due to the picket-fence effect and therefore applying Equation (9) directly on the SES of the signal could lead to suboptimal results. Hence, the following feature is calculated instead

$$\Psi_{prom}(\boldsymbol{f};\boldsymbol{x},\boldsymbol{\alpha},\boldsymbol{\omega}) = \sum_{\alpha\in\boldsymbol{\alpha}} \frac{\max\left\{\mathrm{SES}_{\boldsymbol{x}_{\boldsymbol{f}}^{\varphi}}(\alpha_e)\right\}_{\alpha\cdot(1-c_{tol}/2)\leq\alpha_e\leq\alpha\cdot(1+c_{tol}/2)}}{\mathrm{median}\left\{\mathrm{SES}_{\boldsymbol{x}_{\boldsymbol{f}}^{\varphi}}(\alpha_e)\right\}_{\alpha-1\leq\alpha_e\leq\alpha+1}}, \tag{11}$$

where $\max\left\{\mathrm{SES}_{\boldsymbol{x}_{\boldsymbol{f}}^{\varphi}}(\alpha_e)\right\}_{\alpha\cdot(1-c_{tol}/2)\leq\alpha_e\leq\alpha\cdot(1+c_{tol}/2)}$ indicates that the maximum value of the SES in the range $\alpha\cdot(1-c_{tol}/2)\leq\alpha_e\leq\alpha\cdot(1+c_{tol}/2)$ is used as an estimate of the amplitude of the component-of-interest. The cyclic order tolerance c_{tol} is set to $c_{tol}=0.1$. The denominator of Equation (11) aims to estimate the localised noise level of the SES and uses the median of the SES in the cyclic order band $\alpha-1\leq\alpha_e\leq\alpha+1$. The median is used, because it is more robust to other signal components than the average or the RMS for example [29].

If the rotational speed and the kinematics of the gearbox are unknown, then it is suggested that a blind feature such as the negative entropy should be used [22].

2.2. Initialisation procedure

We need to solve the optimisation problem in Equation (7) using numerical optimisation methods. This requires the optimisation solver to be initialised at a specific point in the design space. The objective function is expected to contain many local maxima, since the rotating machine may have many natural frequencies in the bandwidth of the measured signal. As a result, a random initialisation procedure could result in the optimisation procedure to converge to a local maximum that is not close to the global best.

We therefore propose using a grid-based initialisation procedure to scan the entire frequency range for informative frequency bands. This grid is illustrated in Figure 4. This means that there are several

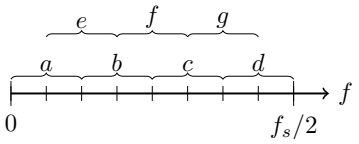

Figure 4: The initialisation procedure is illustrated using seven points evenly spaced between the 0 Hz and Nyquist frequency $f_s/2$ Hz on the spectral frequency axis f. There are seven candidate bandpass filters, denoted a, b, ..., g located between the 0 Hz and $f_s/2$ Hz. If $\Delta f=(f_s/2)/8$, then the spacing between the centres of the bandpass filters is Δf and the bandwidth of the filters is $2\cdot\Delta f$.

candidate bandpass filters on the grid, with the scoring function (e.g. see Figure 3) being calculated for each candidate bandpass filter. Thereafter, the centre frequency of the bandpass filter with the best score is used to initialise the optimisation algorithm. This initialisation procedure ensures that the region of the optimal informative frequency bands are identified and this ensures the success of the subsequent optimisation procedure. The methods proposed in Ref. [23, 25] use a similar procedure to find the informative frequency bands in the signal, however, this was developed for kurtosis-based indices and the subsequent optimisation step, discussed in Section 2.3, is not performed.

This grid-based initialisation procedure is feasible as the design space is two-dimensional (i.e. $\boldsymbol{f}\in\mathbb{R}^2$) and the lower and upper bounds are well-defined (e.g. 0 Hz and $f_s/2$ respectively, where f_s is the sampling frequency). We chose the bandwidth of the filter $\Delta f=100$ Hz and the overlap between two consecutive

grid points equal to 50 Hz in the initialisation process. It is suggested in Ref. [23, 25] that the passband should contain at least three harmonics of the fault component.

2.3. Optimisation procedure

Many optimisation methods utilise gradient information to find a local minimum of the cost function [36]. This requires the calculation of the gradient of the derivative of the score function with respect to the design variables, which is not always possible nor feasible [43, 44]. This makes derivative-free search methods such (e.g. Nelder-Mead algorithm [43], the modified cookoo search algorithm [44], the particle swarm optimisation algorithm [45], the ant colony algorithm [46]) attractive.

Global search methods such as the particle swarm optimisation and the genetic algorithms are generally very computationally expensive and may not convergence to the global minimum [36, 43]. The Nelder-Mead algorithm is a simple local search method that generally performs well in low-dimensional problems [43, 47]. Since it is assumed that a good initial position is obtained in the previous step and the fact that the optimisation problem is two-dimensional, the Nelder-Mead algorithm is well-suited for this search task.

The Nelder-Mead algorithm is performed by sequentially constructing a sequence of simplexes to improve the cost function under consideration [47]. Four possible operations can be performed on the simplex during the optimisation procedure, namely, reflection, expansion, contraction and shrink. The implementation that is available in the Scientific Python (SciPy) library [38] was used in this work with the standard optimisation parameters being used [47]. The tolerance of the absolute error between iterations was set to 10^{-9}. Thorough discussions on the algorithm can be found in Refs. [47], with a short overview given in Appendix A of the different operations that can be performed.

2.4. Bandpass filtering and signal analysis

The optimal frequency band $\boldsymbol{f}$ determined in the previous step is used to design a bandpass filter $\boldsymbol{h}_f$, whereafter the signal under consideration is filtered with Equation (2) to obtain a vibration signal $\boldsymbol{x_f}$ with the fault information enhanced. Subsequently, this filtered signal needs to be further processed to infer the condition of the gearbox. The SES is frequently combined with informative frequency band identification methods (e.g. [23, 27, 29]) for fault detection. The SES of the order tracked filtered signal [17]

$$\mathrm{SES}_{\boldsymbol{x_f}}(\alpha) = \mathcal{F}_{\varphi\to\alpha}\left\{|\boldsymbol{x}_{\boldsymbol{f}}^{\varphi}|^2\right\}, \tag{12}$$

makes it possible to detect periodicities associated with the signal-of-interest in the enhanced vibration signal. The Synchronous Average of the Squared Envelope (SASE) [18]

$$\mathrm{SASE}(\varphi;\Phi) = \frac{1}{N_\Phi}\sum_{k=0}^{N_\Phi-1}|x^\varphi(\varphi+k\cdot\Phi)|^2, \tag{13}$$

makes it possible to visualise the modulation that is caused by the damaged component-of-interest with a cyclic period of Φ. The cyclic period Φ is the reciprocal of the cyclic order of the component-of-interest. The SASE of the angular domain signal $x(\varphi)$ is defined over the domain $\varphi \in [0, \Phi)$ and is estimated over N_Φ rotations of the component-of-interest. The SES can be used to identify the cyclic orders of the cyclostationary components, while the SASE can be used to distinguish between localised and distributed gear damage modes.

In the last step of the condition monitoring process, the processed vibration signal is usually converted into a condition indicator, a scalar metric that can be used to detect changes in the condition of the machine. There are many condition indicators available that can be used for gearbox condition monitoring, such as the root-mean-square, kurtosis, indicators-of-cyclostationarity, and methods based on statistical tests [13, 48]. In this work, we use the score function of the filtered signal

$$\mathrm{CI}(\boldsymbol{\alpha}) = \sum_{\alpha\in\boldsymbol{\alpha}} \frac{\max\left\{\mathrm{SES}_{\boldsymbol{x_f}^\varphi}(\alpha_e)\right\}_{\alpha\cdot(1-c_{tol}/2)\leq\alpha_e\leq\alpha\cdot(1+c_{tol}/2)}}{\mathrm{median}\left\{\mathrm{SES}_{\boldsymbol{x_f}^\varphi}(\alpha_e)\right\}_{\alpha-1\leq\alpha_e\leq\alpha+1}}, \tag{14}$$

as a Condition Indicator (CI). This allows us to monitor how the prominence of the component-of-interest changes over time. The optimisation of the condition indicator is outside the scope of this work.

2.5. Novelty detection

Historical condition monitoring data of a machine operating in a healthy condition is easily acquired when condition monitoring is performed continuously on a machine. This historical data from a healthy machine can therefore be used for automatic fault detection in the form of novelty detection.

We desire to determine a threshold τ that would allow us to determine whether a processed filtered signal $\mathcal{P}\{\boldsymbol{x_f}\}$ is healthy (i.e., $\mathcal{P}\{\boldsymbol{x_f}\} \leq \tau$) or not (i.e., $\mathcal{P}\{\boldsymbol{x_f}\} > \tau$), where $\mathcal{P}\{\cdot\}$ denotes a general processing operator (e.g. calculating the SES with Equation (12), the SASE with Equation (13), or the CI in Equation (14)).

In this work, the threshold of the SASE is a scalar variable, i.e. $\tau_{SASE} \in \mathbb{R}$, while the threshold of the SES is a function of the cyclic order, i.e. $\tau_{SES}(\alpha) \in \mathbb{R}$. The SASE is compared against a scalar, as the healthy SASE of the narrowband signal is expected to be relatively flat and aligning the phase between the measurements could be difficult without a keyphasor on the shaft-of-interest. However, irrespective

of whether the threshold is a scalar or vector, it is expected to be dependent on the frequency band determined in the previous step, i.e. $\tau(\boldsymbol{f})$. Hence, the procedure shown in Figure 5 is used to determine

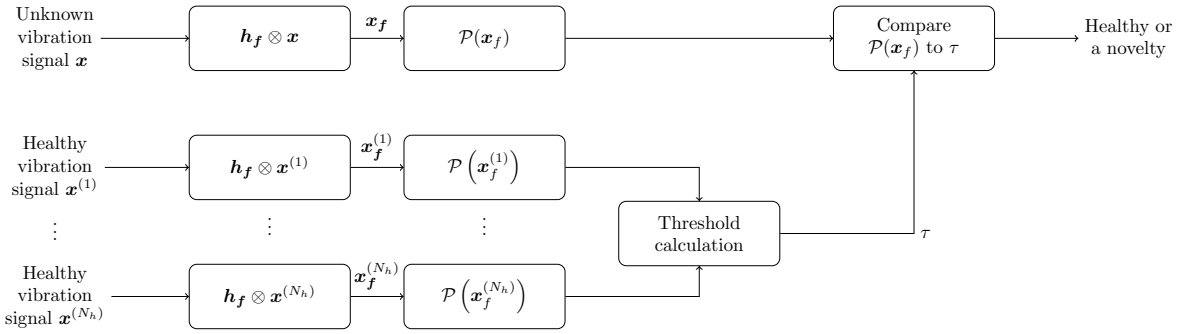

Figure 5: The novelty detection part of the proposed method is presented for a vibration signal $\boldsymbol{x}$, acquired from a rotating machine in an unknown condition. The impulse response function of the filter $\boldsymbol{h_f}$ is determined with the vibration signal $\boldsymbol{x}$ with the procedure shown in Figure 1. The number of healthy measurements is denoted N_h.

a threshold for automatic fault detection and summarised here:

1. For a vibration signal in an unknown condition $\boldsymbol{x}$, identify a frequency band $\boldsymbol{f}$ that maximises a metric (e.g. Equation (11)) and use this band to design the bandpass filter $\boldsymbol{h_f}$ with the procedure shown in Figure 1.
2. Use the impulse response function $\boldsymbol{h_f}$, determined in the previous step, with Equation (2) to filter the vibration signal under consideration and obtain the filtered signal $\boldsymbol{x_f}$.
3. For the N_h signals in the healthy historical dataset, use $\boldsymbol{h_f}$ determined in the first step, to obtain a filtered healthy signals, with the ith filtered healthy signal denoted by $\boldsymbol{x}_{\boldsymbol{f}}^{(i)}$. Therefore, each healthy signal in the historical dataset will be filtered with the same filter as the signal $\boldsymbol{x}$.
4. Process the filtered signal $\boldsymbol{x_f}$ and each of the filtered healthy signals $\boldsymbol{x}_{\boldsymbol{f}}^{(i)}$ with the same operator $\mathcal{P}(\cdot)$, where $\mathcal{P}(\cdot)$ denotes the calculation of the SASE, SES or a CI.
5. Use the processed healthy filtered signals to calculate a threshold and compare this threshold to the signal under consideration to perform automatic fault detection.

It is assumed that the healthy machine operated under approximately the same time-varying operating conditions states as the machine under consideration, e.g. that the healthy operating conditions were not all taken during an idling state and the testing signal is from a full load state.

The threshold for the SASE is calculated by firstly calculating the 99th percentile of the SASE of each filtered healthy signal. Thereafter, the maximum value of the 99th percentile of the healthy signals is calculated and used as a threshold. The 99th percentile at each cyclic order value in the SES of the filtered healthy signal is used to set a cyclic order dependent threshold for the SES. It is suggested that a large number of representative healthy measurements N_h are used when calculating the threshold. This will ensure that a representative threshold is used for the novelty detection.

In the next section, the proposed method is investigated on experimental data acquired under time-varying operating conditions.

3. Experimental investigation

The gearbox test-rig in Figure 6 is located in the Centre for Asset Integrity Management (C-AIM) laboratory of the University of Pretoria and was used to generate the vibration data considered in this work. The test-rig consists of three helical gearboxes, with the centre gearbox (i.e. Gearbox 2 in Figure

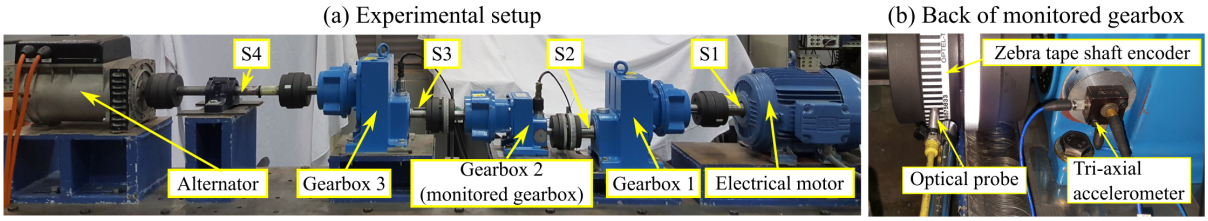

Figure 6: The experimental test-rig that was used to generate the data is presented in (a), with the shafts annotated by $S1$, $S2$, $S3$ and $S4$. The tri-axial accelerometer and the optical probe, which are located on the back of the gearbox, are shown in (b).

6(a)) being monitored for damage. The gearbox is instrumented with a 100 mV/g tri-axial accelerometer, shown in Figure 6(b), with the axial component of the tri-axial accelerometer being used throughout this paper. A closer view of the tri-axial accelerometer is presented in Figure 7.

The vibration signal is sampled at 25.6 kHz and the instantaneous angular speed of the gearbox is estimated with the tachometer signal obtained from the zebra tape shaft encoder and the optical probe highlighted in Figure 6(b). The tachometer signal is sampled at 51.2 kHz. The important frequency bands were not known a priori and therefore the sampling frequency of the vibration signal was selected to the highest feasible value to ensure that damage, which could potentially manifest in high frequencies, can be detected. The informative frequency bands, which depends on the dynamic properties of the system, were

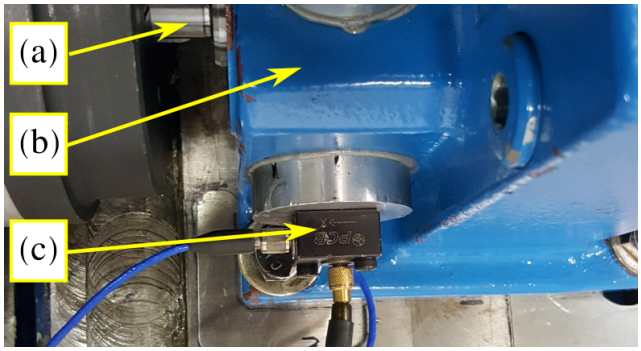

Figure 7: A zoomed view of the tri-axial accelerometer is shown on the back of the gearbox. (a) The input shaft, denoted S2 in Figure 6 of the monitored gearbox; (b) The bearing housing of the monitored gearbox; (c) The top-view of the tri-axial accelerometer.

for example located in a 7 kHz, 13.5 kHz and 23 kHz frequency bands for the different signals considered in Ref. [21]; and the informative frequency band was centred at 11 kHz in Ref. [19]. To ensure that the zero-crossing point of the zebra tape shaft encoder is accurately detected, the highest possible sampling frequencies for the tachometer was selected. The vibration data and tachometer measurements were acquired with an OROS OR 35 data acquisition system. Since the gear is connected to the shaft with the optical probe, it rotates at 1.0 shaft orders. The modulation from the damaged gear is therefore expected to have a cyclic order of 1.0 shaft orders and therefore the targeted cyclic orders are $\boldsymbol{\alpha} = [1.0, 2.0, 3.0]$.

The Weg 5,5 kW three-phase four-pole squirrel cage electrical motor drives the system and the 5.5 kVA Mecc Alte SpA three-phase alternator dissipates the rotational energy, with both being separately controlled with a personal computer. The operating conditions were controlled using predefined functions, with operating conditions that are investigated in this work are shown in Figure 8. Since the maximum

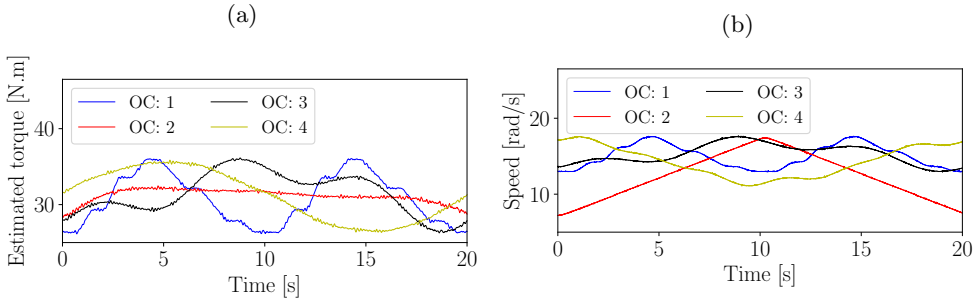

Figure 8: The operating conditions that were estimated at the input shaft of the monitored gearbox. The input shaft of the monitored gearbox is numbered as S2 in Figure 6.

cyclic frequency of the damaged components would be 3 Hz for the experimental dataset, a minimum bandwidth of $\Delta f_{lh} = 20$ Hz in Equation (8) would be sufficient.

In this work, the monitored helical gearbox (i.e. gearbox 2 in Figure 6(a)) was damaged with localised and distributed gear damage. Thirty measurements from a healthy gearbox (i.e. with both the pinion and the gear of the monitored gearbox healthy) are used to calculate the thresholds discussed in Section 2.5 and subsequently used for novelty detection.

In the next section, the proposed method is investigated on data that were acquired from the monitored gearbox where the gearbox had localised gear damage.

3.1. Localised Gear Damage (LGD) investigation

Localised Gear Damage (LGD) was induced in the gear of the monitored gearbox by seeding a slot in its root, with the seeded slot shown in Figure 9(a). The gearbox was operated for approximately 20 days, with the damaged tooth failing in the final stages of the experiment. In Figure 9(b), the gear is shown after the experiment was completed, with the missing tooth clearly seen. The gearbox was operated

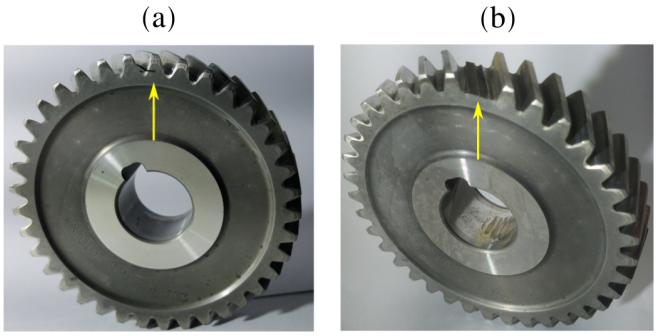

Figure 9: The gear used in the Localised Gear Damage (LGD) investigation is presented. (a) The gear before the experiment started; (b) The gear after the experiment was completed.

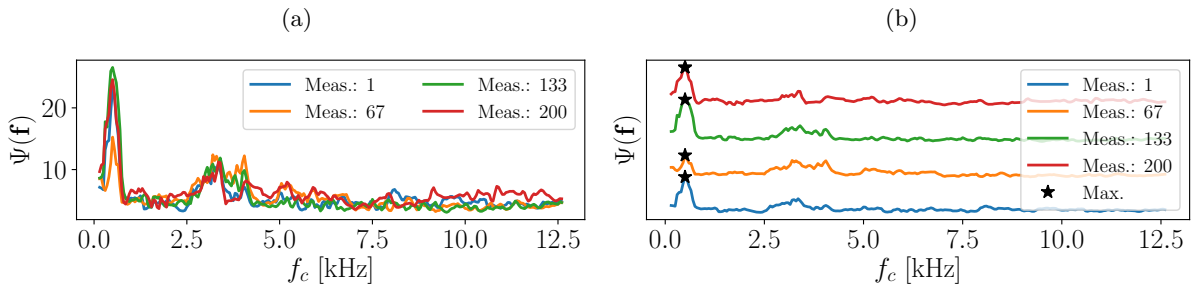

Figure 10: The score function $\Psi(\boldsymbol{f})$, calculated for the frequency band $\boldsymbol{f} = [f_l, f_h]$, is presented over the centre frequency $f_c = (f_h + f_l)/2$ for four measurements of the localised gear damage experiment dataset. The centre frequency that corresponds to the maximum value of each measurement is used to initialise the optimisation algorithm for that measurement. (a) The score function is presented; (b) The actual score function presented in (a) is given an offset to make the results easier to visualise.

under the first operating condition profile in Figure 8 (i.e. OC: 1) during all tests, with 200 measurements acquired between the initial condition (i.e. Figure 9(a)) and the final condition (i.e. Figure 9(b)).

Four condition indicators are shown for the 200 raw signals in Appendix B and illustrates that the degradation of the gear is not easily seen. In addition to this, one of the last signals in the dataset set is decomposed in terms of the damaged component and the impulsive components in the same appendix. The results indicate that even though the gear is severely damaged in the considered measurement, it is very difficult to detect the damage due to the dominant impulsive components.

In the first step of the proposed method, the optimisation algorithm needs to be initialised. This is performed by dividing the spectral frequency axis into a grid of points, whereafter the cost function is evaluated at each point on the grid as shown in Figure 4. The result that was obtained from the grid estimation approach is presented in Figure 10 for different measurements in the localised gear damage dataset. The f_c that maximises the score is used to centre the initial bandpass filter and the bandwidth was selected to be equal to the bandwidth that was used in the grid-initialisation procedure.

The parameters determined from the initialisation procedure are used to initialise the Nelder-Mead optimisation algorithm for each signal in the dataset, whereafter the Nelder-Mead optimisation algorithm

iterated until the change in the design variable $\boldsymbol{f}$ was smaller than the tolerance of 10^{-9}. The initial value of the frequency band and the final value after completing the optimisation procedure are superimposed on the objective function in Figure 11 for two measurements in the dataset. Even though the initialisation

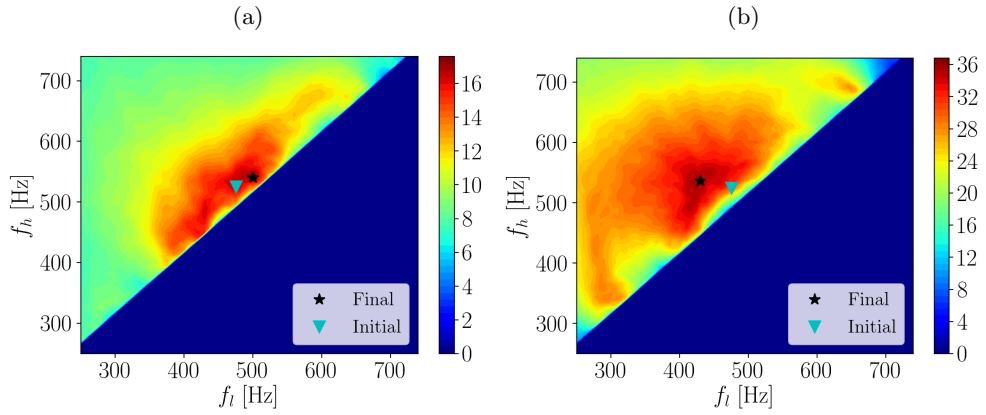

Figure 11: The objective function is shown for two measurements in the localised gear damage experiment, with the initial value and the final value of the optimisation algorithm superimposed on the plot. The initial value is obtained with the initialisation procedure discussed in Section 2.2. In Figures 11(a) and 11(b), the result for the 50th and 75th measurement are respectively shown. The infeasible region was given a value of 0.0 in these plots to make the results easier to visualise. This is possible since the scoring function used in this work is strictly positive.

procedure is capable of finding a very good solution, it is not the optimal solution. The optimisation algorithm is capable of finding the optimal frequency band to enhance the signal components associated with the component-of-interest. Since the damage was more developed in Figure 11(b) compared to Figure 11(a), there is a larger region in the design space with fault information (i.e. a larger red region). Additionally, the results in Figures 10 and 11(b) indicate that there can be many local maxima in the design space and therefore it is critical to perform a thorough initialisation process if a local search or optimisation algorithm is utilised.

The SASE and the SES of the raw and filtered signals are compared in Figure 12 for the measurement considered in Figure 11(a). It is not possible to observe the damaged components in the processed raw signals in Figures 12(a) and 12(c). This is attributed to the signal containing dominant impulsive components that are not linked to the condition of the gear, but rather attributed to a floating bearing. The helical gears have larger contact ratios than spur gears, which means that changes in the condition of a single tooth would be more difficult to detect. This makes it difficult to detect the damage in the raw signals.

In contrast, the results in Figures 12(b) and 12(d) indicate that the proposed method is capable of identifying an informative frequency band, which results in the fault information to be enhanced in the vibration signal. The SASE in Figure 12(b) indicates that there is gear damage in the region of 135 degrees, while the SES indicates that the instantaneous power has a strong periodic component with a

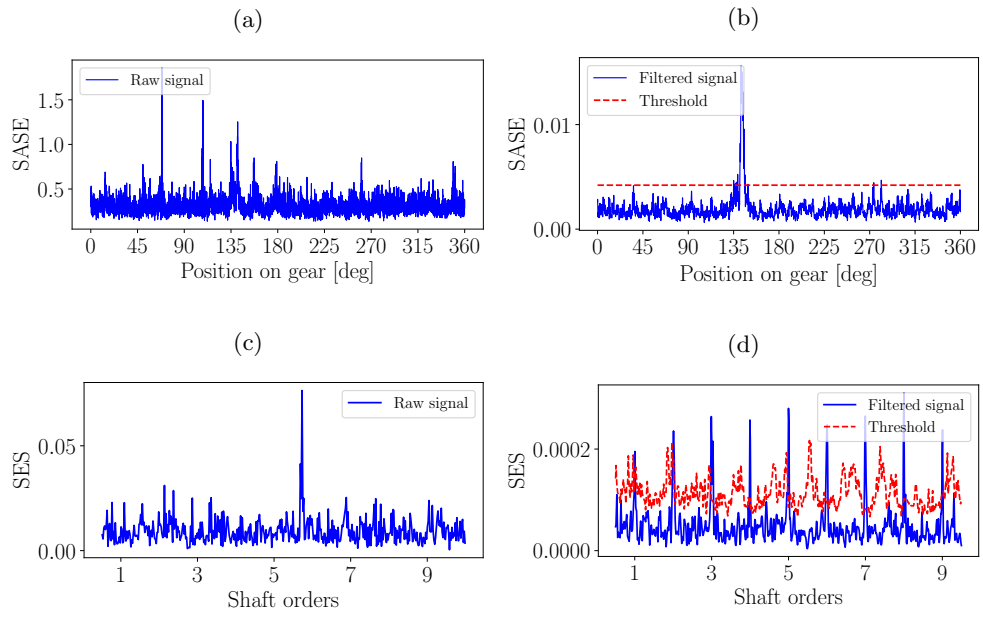

Figure 12: The SASE and SES of the raw and the filtered signals are compared for the 50th measurement of the Localised Gear Damage (LGD) experiment. The threshold was obtained with the procedure discussed in Section 2.5. The objective function of this signal is shown in Figure 11(a).

fundamental order of 1.0 shaft order.

The thresholds, calculated with the procedure discussed in Section 2.5 and shown in Figure 5, are superimposed on the SASE and the SES in Figures 12(b) and 12(d) respectively. This makes it possible to automatically determine which signal components are novel and which components are healthy. In Figure 12(b), the SASE exceeds the threshold in the region of 135 degrees, while the cyclic components associated with the gear components (i.e. 1.0 shaft orders and its harmonics) exceeding the threshold in Figure 12(d).

The results of the second measurement considered in Figure 11(b), where the damaged was more developed, is presented in Figure 13. The damage is much more prominent in Figure 13(a) when compared to the previous signal in Figure 12(a). However, the SASE remains adversely affected by the impulsive noise components. In contrast, the SASE of the filtered signal in Figure 13(b) performs much better, with the damaged component very clearly seen in the region of 135 degrees. The thresholds, shown in Figures 13(b) and 13(d), makes it possible to automatically identify that this component is damaged and makes it easy to visualise that only a localised portion of the gear is damaged. The SES of the raw signal in Figure 13(a) does not contain any evidence that the gear is damaged and is dominated by the strong impulsive component at 5.7 shaft orders. The SES of the filtered signal in Figure 13(d) is very rich with fault information, with the 1.0 shaft order component and its harmonics clearly exceeding the threshold. The thresholds in Figure 13(b) and 13(d) are calculated with the procedure outlined in Figure 5.

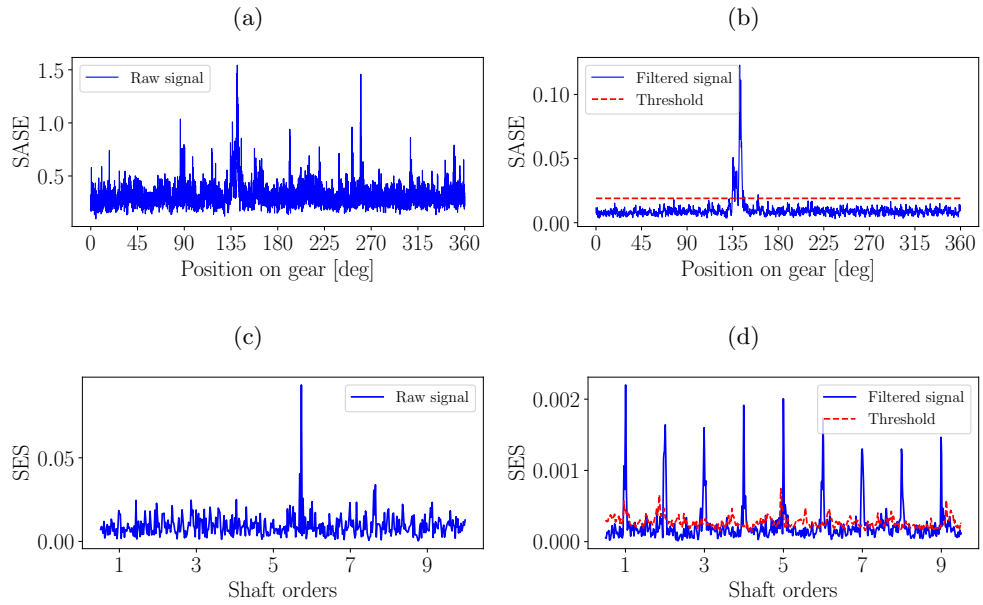

Figure 13: The SES and the SASE are presented for the raw and the filtered signals of the 175th measurement of the Localised Gear Damage (LGD) experiment. The threshold was obtained with the procedure in Section 2.5. The objective function of this signal is shown in Figure 11(b).

The results of ten measurements, evenly spaced over the testing period, are shown in Figures 14. The y-axis, which indicates the measurement number that corresponds to each considered signal, helps to illustrate how the damage develops. The SASE and the SES of the raw signals are presented in Figure 14(a) and 14(c). The SES does not contain any indication that the gear is damaged, with only the impulsive noise component at 5.7 shaft orders clearly seen. The SASE in Figure 14(a) is dominated by the noise components, which makes it difficult to detect the gear damage. The SASE and the SES of the filtered signal, shown respectively in Figures 14(b) and 14(d), contain much fault information. The gear damage is clearly seen in the SASE of the filtered signal and it is possible to see changes in the magnitude of the damaged component as the gear degrades. The 1.0 shaft order component and its harmonics are also very prominent in the SES shown in Figure 14(d), with the change in the condition of the gear also clearly seen.

Hence, the filtering process can enhance the damage information and this makes it possible to detect the damaged gear components. In the next section, the performance of the proposed method is investigated on data that were acquired from a gearbox with damage on the surface of the gear.

3.2. Distributed Gear Damage (DGD) investigation

The gear considered in this section is presented in Figure 15. Only half of the gear teeth (i.e. 180 degrees) were damaged, with the damaged region highlighted in Figure 15(a). This makes it possible to determine whether the damaged region can be detected when using a synchronous representation (e.g.

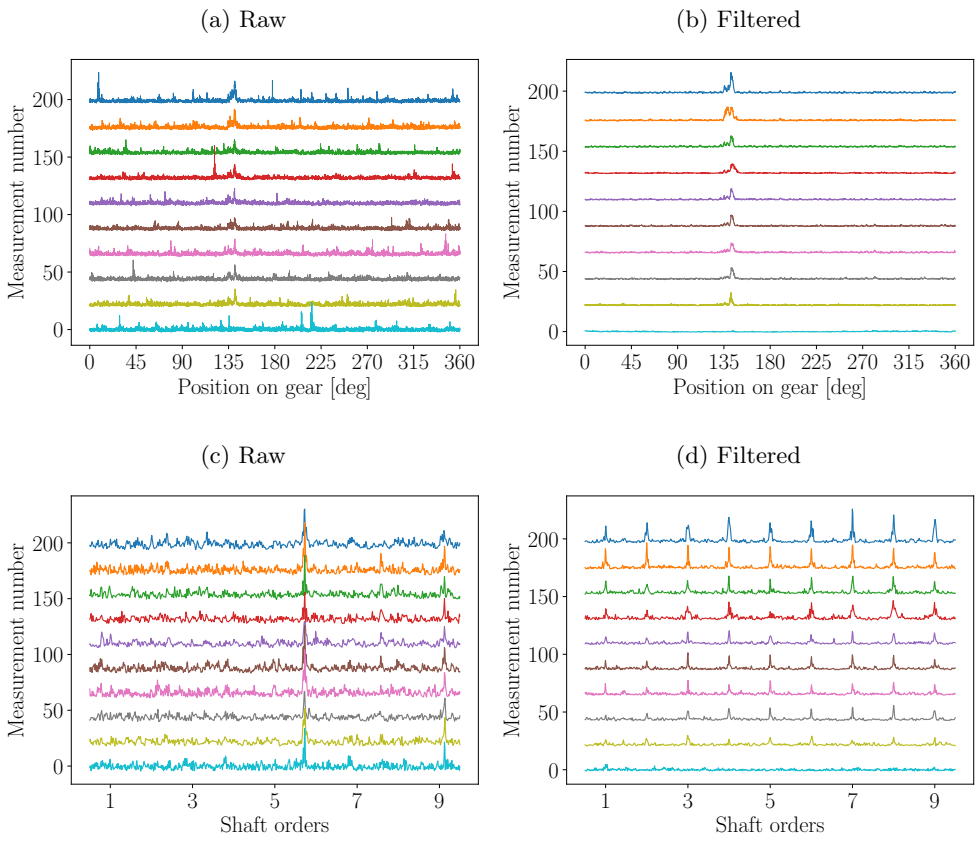

Figure 14: The SASE and the SES are presented over measurement number for the raw and the filtered signals. Since the filtered signals may be associated with different frequency bands and may therefore have different properties (e.g. energy), the SASE and the SES of the filtered signals were normalised with the mean value of the threshold. Each processed SASE and SES were given an offset that is equal to its measurement number; this makes it possible to visualise the changes in the SASE and the SES over measurement number.

SASE). The surface of each gear tooth was damaged with a rotary tool, with the damaged gear teeth shown in Figure 15(b). The gear did not deteriorate during the experiments and therefore the condition of the gear remained the same for the 80 measurements considered in this section. The gears operated periodically under the four operating conditions in Figure 8, i.e. the operating condition sequence was: OC: 1, OC: 2, OC: 3, OC: 4, OC: 1, OC: 2, etc.

The initialisation procedure was implemented on the dataset to find a good initial position, whereafter the Nelder-Mead algorithm was applied to find the maximum value. The initial value and the final solution, obtained with the optimisation procedure, are superimposed on the objective function in Figure 16 for two measurements in the dataset. Since the damage is relatively small and helical gears are used, the damage components are not very prominent in the signal. This results in a very localised region to contain fault information in the design space shown in Figure 16.

The SASE and the SES results are presented in Figure 17 for one of the measurements of the distributed gear damage experiment. The SASE and the SES of the raw signals do not show convincing evidence

Figure 15: The gear that was tested in the Distributed Gear Damage (DGD) experiment. (a) The portion of the gear that is damaged is highlighted; (b) A zoomed view of the damaged gear teeth is presented.

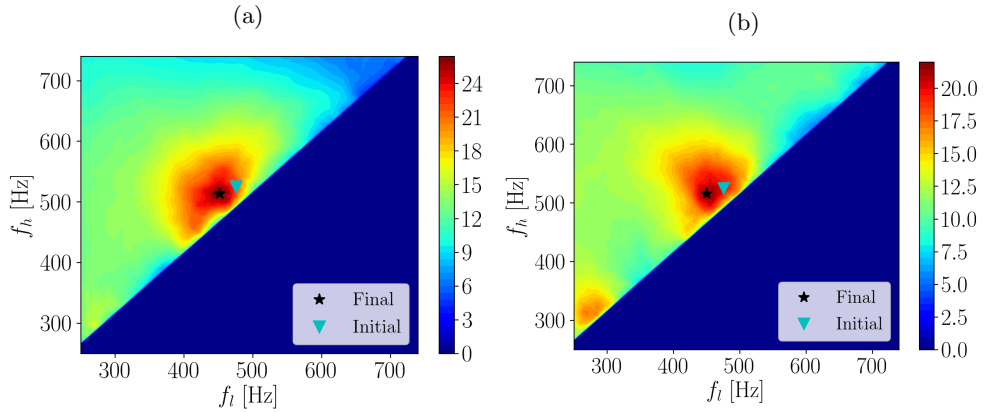

Figure 16: The objective function is shown for two measurements in the distributed gear damage experiment, with the initial value and the final value of the optimisation algorithm superimposed on the plot. In Figures 11(a) and 11(b), the result for the 20th and 30th measurement are respectively shown. The infeasible region was given a value of 0.0 in these plots to make the results easier to visualise. This is possible since the scoring function considered in this work is strictly positive.

that the gear is damaged; the SASE contains much noise over the circumference of the gear in Figure 17(a) and the SES only contains a feint component at 1.0 shaft order in Figure 17(c). In contrast, the SASE and the SES of the filtered signal display much evidence that the gear is damaged. In Figure 17(b), the SASE exceeds the threshold between 135 and 315 degrees, while the SES in Figure 17(d) shows very dominant components at 1.0 shaft orders and its harmonics. The threshold facilitates damage detection, as it is easier to identify the damaged components when comparing the data to the threshold.

The processed results of ten measurements of the first distributed gear damage experiment are presented in Figure 18 over measurement number. The SASE of the raw vibration signal does not show much evidence that a portion of the gear is damaged. While the SES of the raw signal has a 1.0 shaft order component for some measurements, it does not clearly indicate that it is damaged.

The SASE and the SES of the filtered signal in Figures 18(b) and 18(d) contain much evidence that the gear is damaged; the damaged portion of the gear is observed between 135 and 315 degrees in Figure 18(b) and the 1.0 shaft order component and its harmonics are very prominent in the SES shown in Figure 18(b).

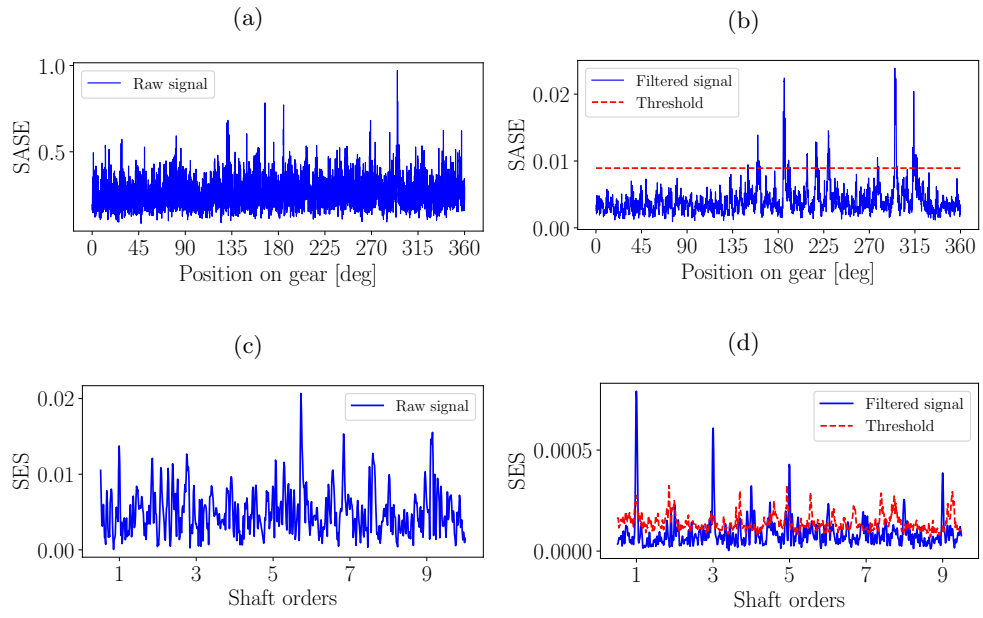

Figure 17: The SES and the SASE are presented for the raw and the filtered signals of the 20th measurement of the Distributed Gear Damage (DGD) experiment. The threshold was obtained with the procedure in Section 2.5. The objective function of this signal is shown in Figure 16(a).

Hence, it is possible to enhance the damaged components in the signal and it is possible to identify the damaged region of the gear. In the next section, the condition indicator is calculated for the two datasets.

3.3. Condition Indicator (CI)

Ultimately, a CI of the processed signal can be used to monitor the condition of the different components of the rotating machine. We calculated the CI in Equation (14) for each measurement in the damaged datasets as well as each measurement in the healthy dataset, with the results presented in Figure 19. At each measurement, the healthy data are filtered with the same filter as the corresponding damaged measurement as shown in Figure 5. This makes the 99th percentile threshold shown in Figure 19 a function of measurement number.

The localised gear damage results in Figure 19(a) indicate that initially the healthy and the damaged condition indicators overlapped. This is attributed to the fact that helical gears were used with a relatively small slot in the teeth. As the gear degrades, the distance between the CI of the damaged measurements and the corresponding CI of the healthy measurements increases, with the damaged measurements exceeding the threshold.

Since the condition of the gearbox remained the same over measurement number for the distributed gear damage case, it would not be possible to see a degrading gear in Figure 19(b). However, the damaged and healthy CI are separated, with the damaged CI exceeding the threshold. Since the bandwidth of the bandpass filter is a function of measurement number (e.g. see Figure 20), the behaviour of the healthy

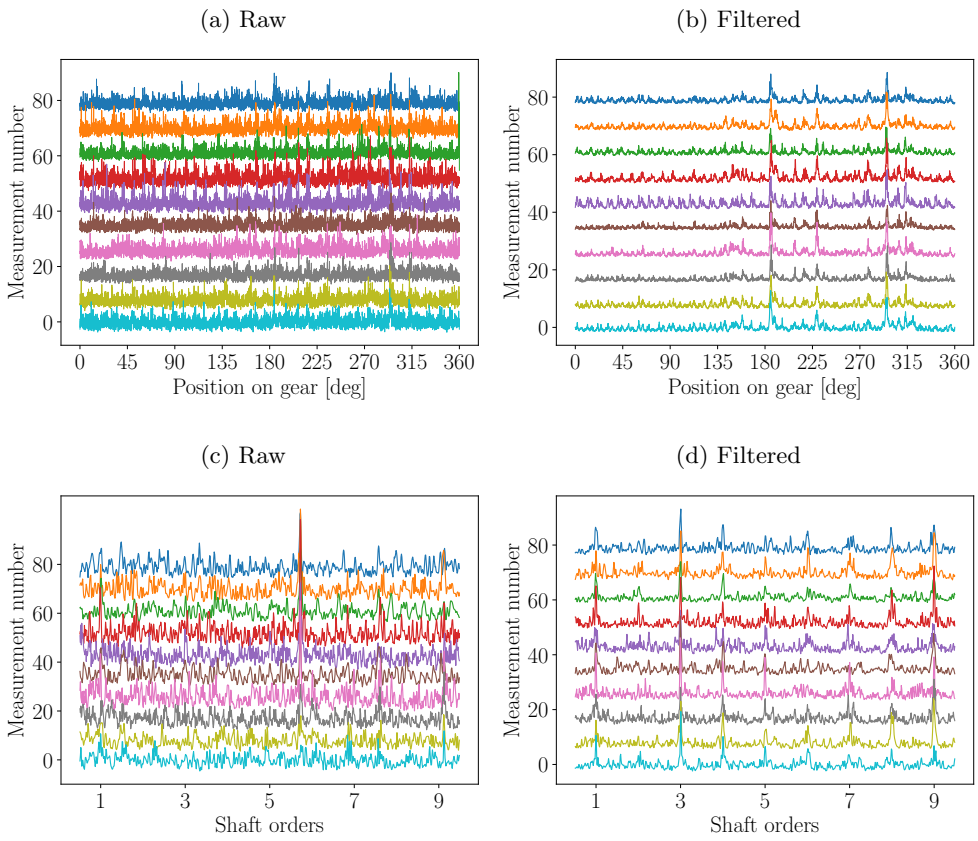

Figure 18: The SASE and the SES are presented over measurement number for the raw and the filtered signals of the distributed gear damage dataset. Since the filtered signals may be associated with different frequency bands and may therefore have different properties (e.g. energy), the SASE and the SES of the filtered signals were normalised with the mean value of the threshold of the signal. Each processed SASE and SES were given an offset that is equal to its measurement number; this makes it possible to visualise the changes in the SASE and the SES over measurement number.

signals and the associated thresholds changes with measurement number.

In the next section, the identified frequency bands, the percentage improvement that is obtained with the optimisation procedure and the computational time are summarised.

3.4. Summary of results

The identified frequency bands is shown in Figure 20 as a function of measurement number for the two datasets. Initially, the localised gear damaged dataset was dominated by a frequency band approximately centred at 3.2 kHz, whereafter the frequency bands centred approximately at 500 Hz was identified as the damage progressed. In Figure 20(b), approximately the same frequency band in the region of 500 Hz was identified for each measurement in the dataset. It is evident from the results in Figure 20 that the informative frequency band can change over time. Since the properties of the signals (e.g. energy) and its condition indicators could be dependent on the frequency band $\boldsymbol{f}$, it makes sense to calculate a new threshold for each signal under consideration with the procedure discussed in Section 2.5.

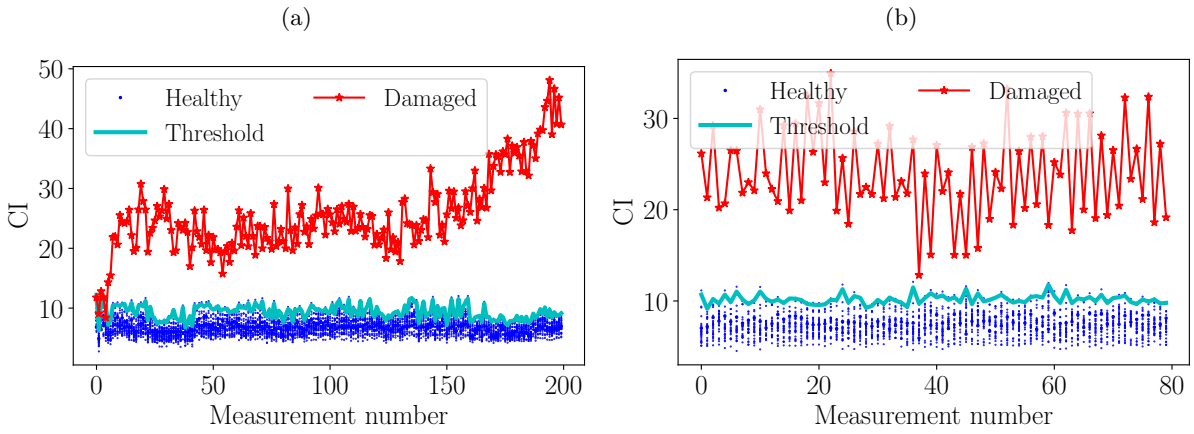

Figure 19: The Condition Indicator (CI), calculated with the filtered vibration signal, is presented for the two damaged gearbox datasets over measurement number. The corresponding CI of the healthy measurements, with its 99th percentile used as the threshold, is presented as well. (a) Localised gear damage experiment; (b) Distributed gear damage experiment.

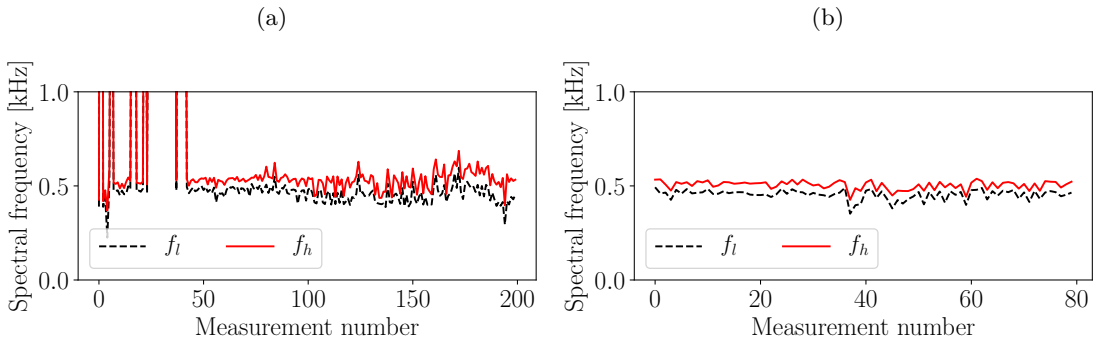

Figure 20: The final frequency band $\boldsymbol{f} = [f_l, f_h]$ that was obtained after applying the optimisation algorithm is presented in (a) for the localised gear damage experiment and in (b) for the distributed gear damage experiment.

The percentage improvement

$$\text{PI} = (\kappa(\boldsymbol{f}_f) - \kappa(\boldsymbol{f}_i))/\kappa(\boldsymbol{f}_i), \tag{15}$$

in the objective function when performing the additional optimisation step is presented in Figure 21 for the two datasets. In Equation (15), the unconstrained objective function, defined in Equation (8), is denoted by κ, the frequency band obtained by the initialisation scheme is denoted by $\boldsymbol{f}_i$ and the final frequency band, obtained after the optimisation procedure was completed, is denoted by $\boldsymbol{f}_f$. The results in Figure 21 indicates that even though the initialisation scheme can find a good frequency band, the additional optimisation step improved the objective function up to 50%.

The median time of the different steps of the calculation are presented in Table 1. The signal needs to be order tracked in each function evaluation, which makes the function evaluations more expensive to calculate. The initialisation procedure searches the whole frequency range for informative frequency bands, which ensures that a good starting position is used in the optimisation algorithm. The computational

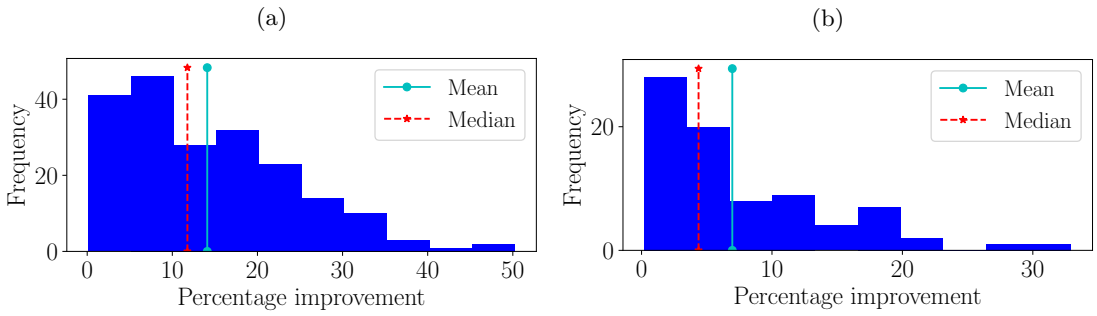

Figure 21: The percentage improvement in the cost function after applying the optimisation algorithm is presented in (a) for the localised gear damage experiment and in (b) for the distributed gear damage experiment. The percentage improvement is calculated with Equation (15).

Table 1: The average time needed to perform the initialisation and optimisation procedures is presented for each measurement in the Localised Gear Damage (LGD) and Distributed Gear Damage (DGD) experiments. The total time is defined as the average duration of both the initialisation and the optimisation parts. The results were calculated in Python 3.7.3 with SciPy 1.3.0 on a personal computer with 32 Gb of RAM and an AMD Ryzen 7 2700x eight-core processor.

	Initialisation [s]	Optimisation [s]	Total [s]
LGD	45.4809	23.8309	69.3118
DGD	62.0048	27.7201	89.7249

time shown in Figure 1 is acceptable for condition monitoring applications.

In the next section, the proposed method is compared against some of the existing frequency band identification methods.

4. Comparison with existing FBI methods

There are many frequency band identification methods available that are suited for vibration signals, e.g. Refs. [21, 22, 26, 27]. The kurtogram is a very popular blind frequency band identification method for bearing and gear fault diagnosis [19–21] and is therefore considered in this work. The kurtogram is constructed by calculating the kurtosis of different bandlimited signals, with the bandlimited signals usually obtained from the short-time Fourier transform [20] or the wavelet packet transform [21]. The kurtosis is a measure of impulsiveness and can therefore be used to identify frequency bands with much impulsive content. Hence, the frequency band with the most impulsive information would maximise the kurtogram.

The kurtogram, calculated using the short-time Fourier transform-based estimator, is used to identify the frequency band with the most impulsive information for each signal considered in this work. The results of the kurtogram are presented in Figure 22 for the localised and distributed gear damage datasets. Since the vibration signals contain much impulsive information not related to the condition of the gears, the kurtogram is maximised by the wrong frequency band. The resulting bandlimited signals do not contain any fault information signals and therefore the damage cannot be detected using the SASE and the SES

in Figure 22. The kurtogram is rather maximised by the impulsive noise component with a cyclic order

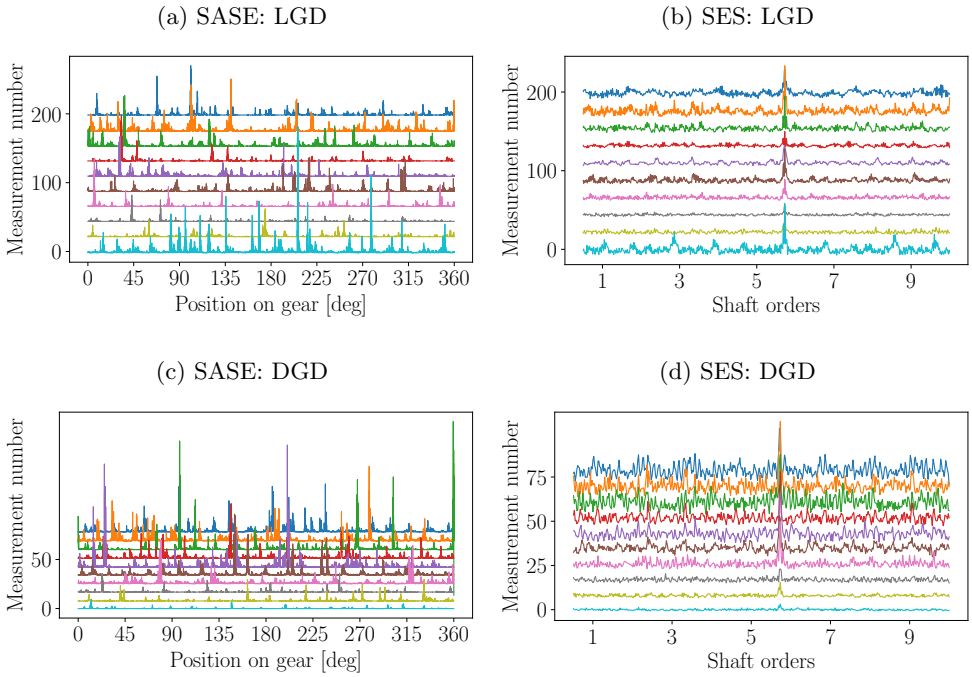

Figure 22: The Synchronous Average of the Squared Envelope (SASE) and the Squared Envelope Spectrum (SES), obtained by using the kurtogram to design a bandpass filter, are presented for the Localised Gear Damage (LGD) and Distributed Gear Damage (DGD) investigations. Each SASE and SES were given an offset that is equal to its measurement number; this makes it possible to visualise the changes in the SASE and the SES over measurement number.

of 5.7, which is very prominent in the SES in Figures 22(b) and 22(d). Since this impulsive component is non-synchronous with the rotation of the gear, it is randomly scattered over the circumference of the gear in Figures 22(a) and 22(c). The improved kurtogram, which uses a wavelet packet decomposition instead of the short-time Fourier transform, was also applied on these signals, but similar results were obtained as the standard kurtogram and therefore excluded for the sake of brevity.

However, the kurtogram cannot distinguish between periodic impulses and random impulses and therefore the ICS2gram is investigated. The ICS2gram is a targeted frequency band identification method that uses an indicator-of-cyclostationarity to identify which frequency bands contain cyclostationary information due to damaged machine components [27]. The indicator-of-cyclostationary is calculated for the gear component, i.e. $\boldsymbol{\alpha} = [1.0, 2.0, 3.0]$, in the different frequency bands of the vibration signal and is maximised to find the optimal frequency band for fault diagnosis. Each bandlimited signal is order tracked to reduce the smearing of the cyclic components due to changes in the speed of the machine. The SASE and the SES are presented in Figure 23 for the bandlimited signals obtained by the ICS2gram. The results in Figures 23(a) and 23(b) indicate that it is possible to detect the gear damage for only one of the ten measurements, while the distributed gear damage cannot be detected in Figures 23(c) and 23(d).

The condition indicators obtained with the proposed method, the kurtogram and the ICS2gram are

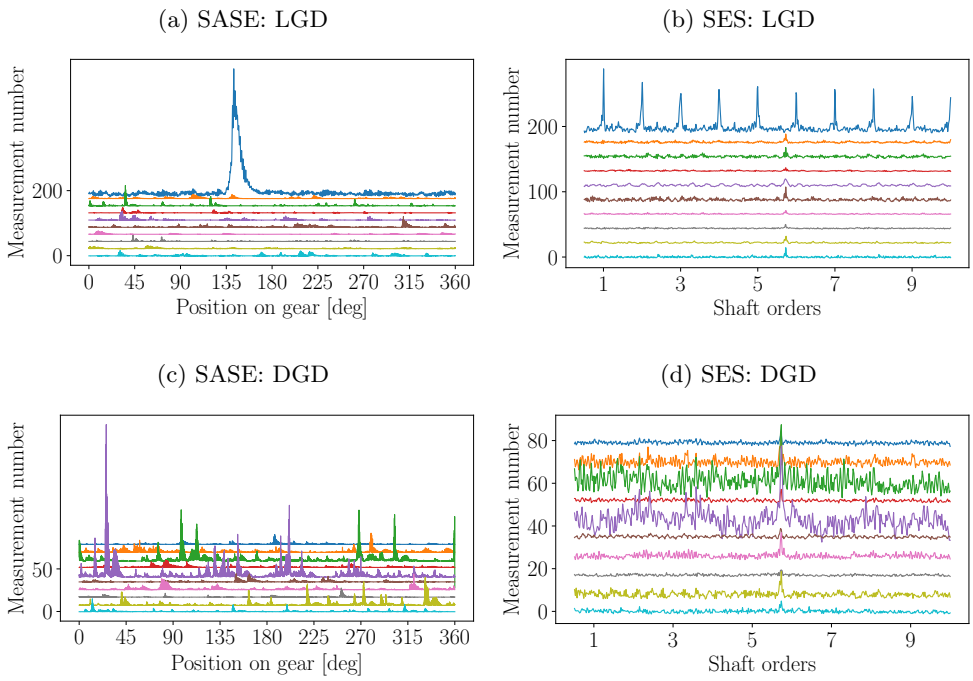

Figure 23: The Synchronous Average of the Squared Envelope (SASE) and the Squared Envelope Spectrum (SES), obtained by using the ICS2gram to design a bandpass filter, are presented for the Localised Gear Damage (LGD) and Distributed Gear Damage (DGD) investigations. Each SASE and SES were given an offset that is equal to its measurement number; this makes it possible to visualise the changes in the SASE and the SES over measurement number.

compared in Figure 24(a) for the localised gear damage experiment. The deterioration of the gear is not identified for the kurtogram in Figure 24(a). This is attributed to the kurtogram not selecting the appropriate frequency bands for fault diagnosis. Even though the results in Figure 23 indicate that the ICS2gram performed poorly to extract the fault information in the signal, two events are seen for its corresponding condition indicator in Figure 24(a). The initial deterioration of the gear tooth is seen in the region of the 25th measurement and the imminent failure of the gear tooth is seen in the region of the 160th measurement of the ICS2gram. Even though these two events are clearly seen, the condition indicator fluctuates significantly at these events (i.e. it is not very robust) and the deterioration of the gear tooth is not seen. Hence, the proposed method performs much better.

The SES of the bandlimited signals are presented for three measurements of the methods considered in Figures 24(b) - 24(d). The damaged components are clearly seen for the proposed method, while in contrast, no damage is seen in the ICS2gram and the kurtogram.

Hence, the conventional methods fail to detect the gear damage investigated in this work. This is attributed to the dominant impulsive components in the signal and to the use if helical gears, which have larger contact ratios than spur gears, that mask the damaged components.

The computational time of the two methods is summarised in Table 2. Even though the proposed method is on average between five and seven times slower than the conventional methods considered in

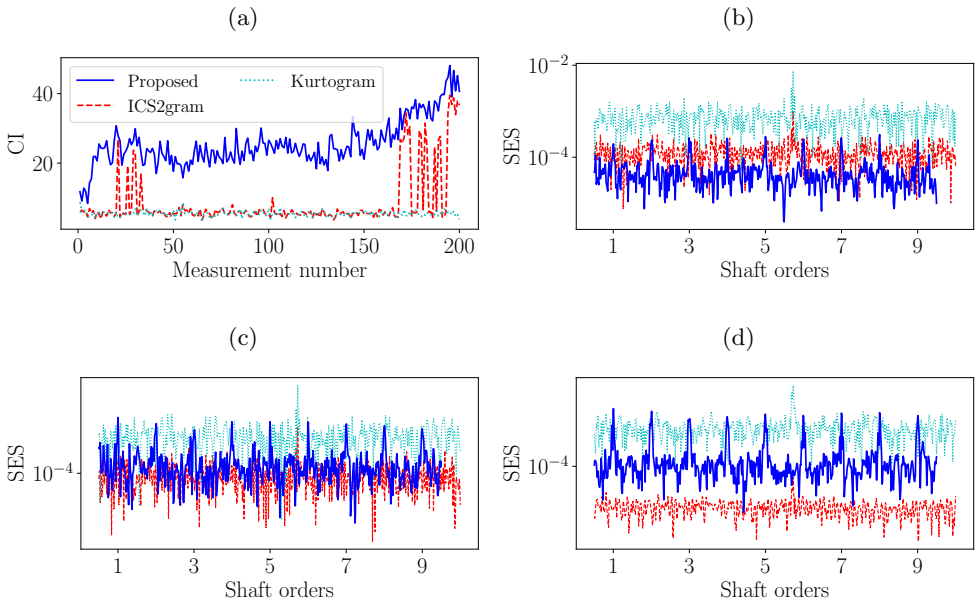

Figure 24: The Condition Indicators (CI), calculated with the bandlimited signals obtained with the Proposed method, the Kurtogram and the ICS2gram, are presented for the Localised Gear Damage (LGD) dataset in Figure 24(a). The SES of measurements 49, 124, and 199 are compared in Figures 24(b) - 24(d) respectively. The same legend is used for all plots.

Table 2: The average time needed to perform find the frequency band with the kurtogram and the ICS2gram for each measurement in the Localised Gear Damage (LGD) and Distributed Gear Damage (DGD) experiments. The results were calculated in Python 3.7.3 with SciPy 1.3.0 on a personal computer with 32 Gb of RAM and an AMD Ryzen 7 2700x eight-core processor.

	Kurtogram	ICS2gram
LGD	12.036 [s]	12.871 [s]
DGD	11.974 [s]	13.470 [s]

this section, it performs much better on the signals considered.

5. Conclusions

The proposed method aims to solve two problems in rotating machine vibration-based condition monitoring; finding optimal frequency bands under time-varying operating conditions and combining this information with healthy historical data for automatic fault detection. The proposed method was applied to two datasets where it was shown that

- it is possible to enhance the weak fault information in the vibration signals under time-varying operating conditions;
- it is possible to utilise the historical data for determining a threshold;
- the threshold, which is dependent on the identified informative frequency band, can be used for automatic fault detection under time-varying operating conditions;

- the cyclic orders of the novel components can be determined with the SES. The SASE makes it possible to determine which portion of the gear is damaged.

Furthermore, the comparison with existing methods highlights the potential of the proposed method under time-varying operating conditions.

Future investigations will include a comparison between different score functions, a comparison of evolutionary algorithms and gradient-based methods for finding the optimal frequency band within the framework of the proposed method, and a comparison of different condition indicators for fault trending also need to be investigated. It is also lastly recommended that the suitability of using acoustic measurements instead of vibration measurements should be investigated. This is because the literature review indicated that acoustic emission signals could indicate earlier signs of damage.

Acknowledgements

S. Schmidt gratefully acknowledges the Eskom Power Plant Engineering Institute (EPPEI) for their support in the execution of this research.

Appendix A. Overview of the Nelder-Mead algorithm

The Nelder-Mead algorithm is a gradient-free minimisation algorithm. The purpose of the frequency band identification problem is to find the frequency band $\boldsymbol{f} \in \mathbb{R}^2$ that maximises the unconstrained cost function given by Equation (8) and denoted $\kappa(\boldsymbol{f})$. This unconstrained maximisation problem can be written as an unconstrained minimisation problem

$$\min_{\boldsymbol{f}} q(\boldsymbol{f}), \tag{A.1}$$

by setting $q(\boldsymbol{f}) = -\kappa(\boldsymbol{f})$. The Nelder-Mead algorithm consists of reflection, expansion, outer contraction, inner contraction and shrink steps [47]. The different operations are shown in Figure A.25 for a simplex with three vertices $\boldsymbol{f}_1$, $\boldsymbol{f}_2$, $\boldsymbol{f}_3$ and explained hereafter.

For this two-dimensional optimisation problem, the simplex has three vertices $\boldsymbol{f}_1$, $\boldsymbol{f}_2$, and $\boldsymbol{f}_3$, that are always sorted such that [47]

$$q(\boldsymbol{f}_1) \leq q(\boldsymbol{f}_2) \leq q(\boldsymbol{f}_3), \tag{A.2}$$

with the centroid of the two best vertices calculated with

$$\bar{\boldsymbol{f}} = \frac{1}{2} \cdot (\boldsymbol{f}_1 + \boldsymbol{f}_2)\,. \tag{A.3}$$

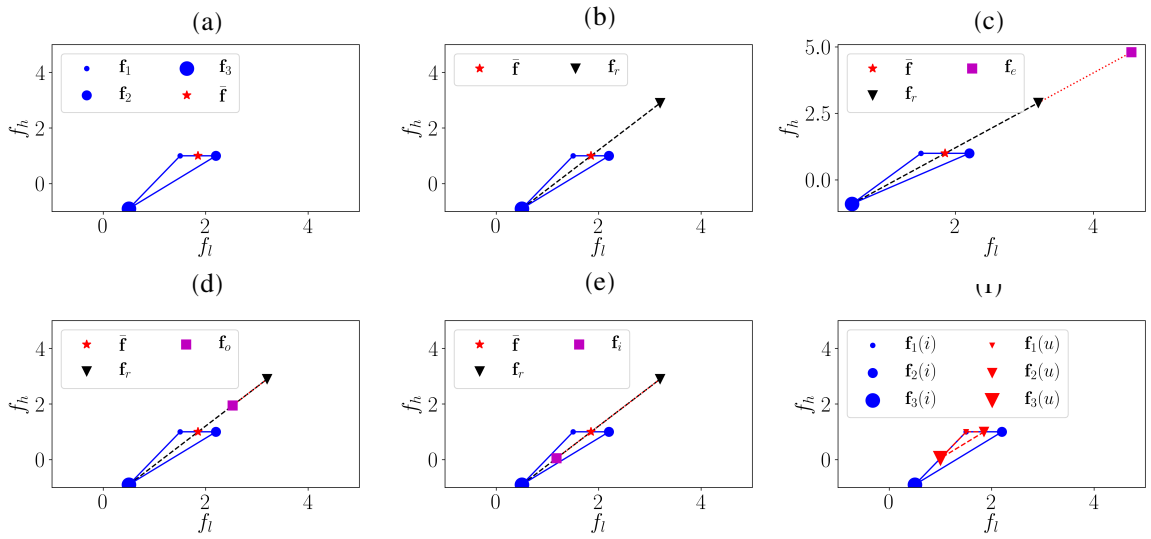

Figure A.25: The different operations of the Nelder-Mead algorithm are illustrated for a simplex in a two-dimensional space. The mth vertex of the original simplex is denoted $\boldsymbol{f}_m(i)$ and the mth vertex of the updated simplex is denoted $\boldsymbol{f}_m(u)$. The size of the markers indicates the relative size of the cost function values, i.e. a larger marker is at a worse location compared to a small marker. The vertices are ordered according to Equation (A.2). (a) Initial simplex with centroid $\bar{\boldsymbol{f}}$; (b) Reflection point; (c) Expansion point; (d) Outside contraction; (e) Inner contraction; (f) The simplex after a shrink operation. The values of the axes are not sensible for the frequency band identification problem, but used for demonstration purposes.

The centroid is superimposed on the simplex in Figure A.25, by assuming the vertex $\boldsymbol{f}_3$ has the largest function value. In the next step, a reflection point is calculated which is collinear with the vertex $\boldsymbol{f}_3$ and the centroid $\bar{\boldsymbol{f}}$ [47]:

$$\boldsymbol{f}_r = \bar{\boldsymbol{f}} + \beta_a \cdot \left(\bar{\boldsymbol{f}} - \boldsymbol{f}_3\right), \tag{A.4}$$

with the scalar $\beta_a \in \mathbb{R}^+$ governing the size of the reflection step. This procedure is shown in Figure A.25(b) by using the centroid from Figure A.25(a) and $\beta_a = 1.0$. The reflection point replaces the worst vertex $\boldsymbol{f}_3$ if $q(\boldsymbol{f}_1) \leq q(\boldsymbol{f}_r) < q(\boldsymbol{f}_2)$. Otherwise, the following operations are performed depending on the function values [47]:

- If $q(\boldsymbol{f}_r) < q(\boldsymbol{f}_1)$, then an expansion operation needs to be performed, with the expansion point calculated with

$$\boldsymbol{f}_e = \bar{\boldsymbol{f}} + \beta_b \cdot \left(\boldsymbol{f}_r - \bar{\boldsymbol{f}}\right), \tag{A.5}$$

  where $\beta_b \in \mathbb{R}^+$ is a coefficient that governs the magnitude of the expansion step. This expansion point is shown in Figure A.25(c) for $\beta_b = 2.0$. If $q(\boldsymbol{f}_e) < q(\boldsymbol{f}_r)$ then the worst vertex $\boldsymbol{f}_3$ is replaced with the expansion point, otherwise the worst vertex is replaced with the reflection point $\boldsymbol{f}_r$ to obtain a new simplex [47].

- If $q(\boldsymbol{f}_2) \leq q(\boldsymbol{f}_r) < q(\boldsymbol{f}_3)$, an outer contraction point needs to be calculated with [47]

$$\boldsymbol{f}_o = \bar{\boldsymbol{f}} + \beta_c \cdot \left(\boldsymbol{f}_r - \bar{\boldsymbol{f}}\right), \tag{A.6}$$

  where $\beta_c \in \mathbb{R}^+$. This operation is shown in Figure A.25(d) for $\beta_c = 0.5$. If the outer contraction point is better than the reflection point, then it replaces the worst vertex, i.e. $q(\boldsymbol{f}_3)$, to form a new simplex. Otherwise, a shrink operation needs to be performed as described below.

- If $q(\boldsymbol{f}_r) \geq q(\boldsymbol{f}_3)$, an inside contraction point needs to be calculated with [47]

$$\boldsymbol{f}_i = \bar{\boldsymbol{f}} - \beta_c \cdot \left(\boldsymbol{f}_r - \bar{\boldsymbol{f}}\right), \tag{A.7}$$

  which is shown in Figure A.25(e). If the inner contraction point is better than the worst vertex, then it replaces the worst vertex, i.e. $q(\boldsymbol{f}_3)$; otherwise a shrink operation needs to be performed as outlined below.

- If a shrink step is necessary according to the outer contraction or inner contraction steps, then the following steps need to be followed [47]:

$$\boldsymbol{f}_2 = \boldsymbol{f}_1 - \beta_d \cdot (\boldsymbol{f}_2 - \boldsymbol{f}_1) \tag{A.8}$$

$$\boldsymbol{f}_3 = \boldsymbol{f}_1 - \beta_d \cdot (\boldsymbol{f}_3 - \boldsymbol{f}_1), \tag{A.9}$$

  where $\beta_d \in \mathbb{R}^+$. This operation is shown in Figure A.25(f) with $\beta_d = 0.5$.

This process is then repeated until convergence is reached. A more detailed overview of the algorithm and its implementation are given in Refs. [47] and [38] respectively. The following coefficients are suggested and used in the algorithm: $\beta_a = 1.0$, $\beta_b = 2.0$, $\beta_c = 0.5$, $\beta_d = 0.5$ [47] and the simplex is initialised within the default procedure in Ref. [38].

Appendix B. Raw results

Different statistics of the experimental signals of the localised gear damage experiment are presented in Figure B.26. Only the kurtosis and the L2/L1-norm contain an indication at the 150th measurement that the gear is deteriorating. Hence, it is difficult to use the statistics of the raw signals for damage detection.

The 190th measurement (out of 200) of the localised gear damage dataset is analysed in more detail to highlight the damaged gear components and dominant impulsive components unrelated to the condition

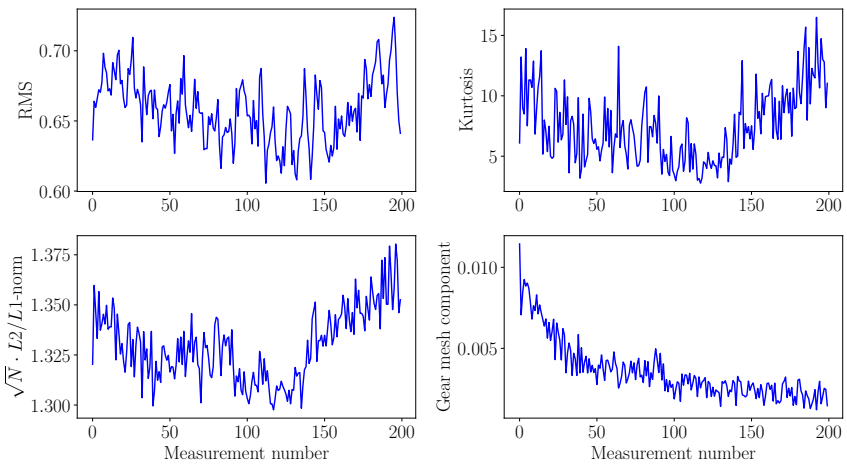

Figure B.26: The Root-Mean-Square (RMS), the Kurtosis, the ratio of the L2 and L1 norms, denoted L2/L1, and the amplitude of the gear mesh component in the spectrum are presented for the localised gear damage experiment. The length of the vibration signal is denoted N.

of the gears. The raw vibration signal denoted by $x[n]$; the vibration signal filtered around an impulsive frequency band without information related to the damage gear denoted by $x[n, f_{l,1}, f_{h,1}]$; and lastly, the vibration signal filtered around the band with the damaged gear information denoted by $x[n, f_{l,2}, f_{h,2}]$ are presented in Figure B.27 with different statistics of the signals shown in Table B.4.

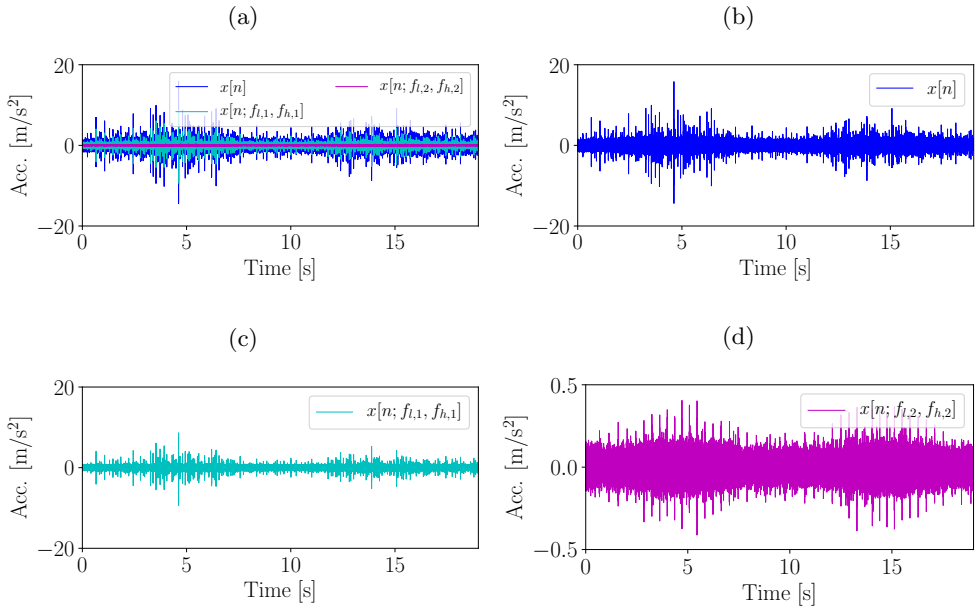

Figure B.27: The raw vibration signal $x[n]$, the signal filtered around an impulsive band $x[n, f_{l,1}, f_{h,1}]$, and the signal filtered around the band with fault information $x[n, f_{l,2}, f_{h,2}]$ are superimposed on the same plot and presented in separate plots as well. Please take note of the different y-axis scaling. B.27(a) is used to show the relative scaling of the different signals.

The results indicate that the time domain signal is dominated by impulsive components unrelated to the damaged gear component. The damaged gear component $x[n, f_{l,2}, f_{h,2}]$ is much less impulsive than the impulsive signal component $x[n, f_{l,2}, f_{h,2}]$ and it only contributes to 0.8494% of the energy of the

Table B.3: More information pertaining to the different signals shown in Figure B.27

Signal	$f_{l,i}$	$f_{h,i}$	Notes
$x[n]$	-	-	Raw signal
$x[n, f_{l,1}, f_{h,1}]$	7.0 kHz	9.0 kHz	Non-gear related impulsive component.
$x[n, f_{l,2}, f_{h,2}]$	450 Hz	500 Hz	Damaged gear component.

vibration signal. This low energy level is attributed to the fact that the damage manifest in a narrow frequency band and the helical gears attenuate the damaged gear components. Ultimately, the weak damage information and the impulsive signal components impede fault detection.

The SES shown in Figure B.4 highlights the low energy level of the damaged gear signal $x[n, f_{l,2}, f_{h,2}]$ and the dominance of the impulsive component $x[n, f_{l,1}, f_{h,1}]$. Since the gear is located on the reference shaft, it has a periodicity of 1.0 shaft order. The impulsive noise components have a periodicity of 5.72 shaft orders, which are clearly seen in the SES of the raw signal and the SES of the impulsive signal $x[n, f_{l,1}, f_{h,1}]$. The amplitude of the damaged component in the SES is at least 50 times smaller than the

Table B.4: The statistics are presented for one of the measurements of the gearbox with localised gear damage. The excess kurtosis is 0.0 for Gaussian signals. The % Energy is calculated as follows: $E_{signal}/E_{raw} \cdot 100$, where E_{signal} is the energy of the signal under consideration and E_{raw} is the energy of the raw signal $x[n]$.

Statistic	$x[n]$	$x[n, f_{l,1}, f_{h,1}]$	$x[n, f_{l,2}, f_{h,2}]$
Excess kurtosis	5.8555	10.5561	1.2589
RMS	0.6277	0.3083	0.0578
% Energy	100.0%	24.1192%	0.8494%

amplitude of the impulsive component.

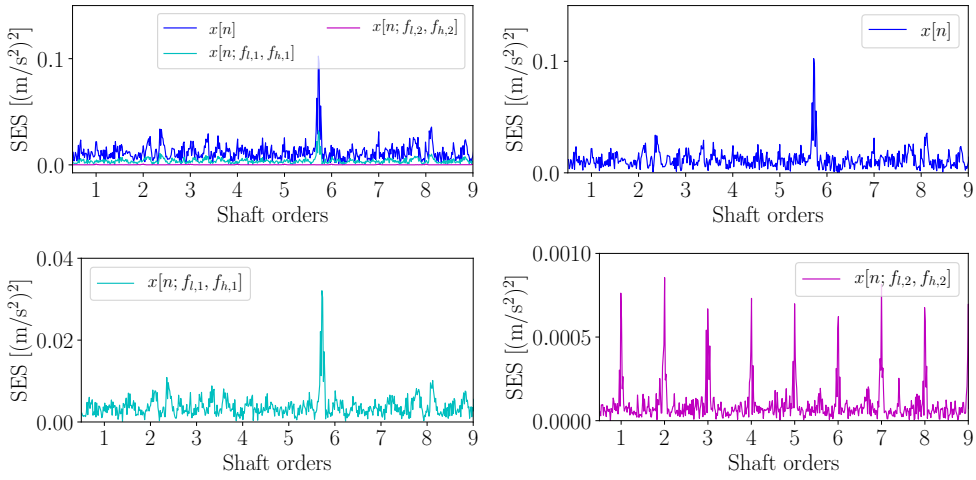

Figure B.28: The SES of the raw vibration signal $x[n]$, the SES of the signal filtered around an impulsive band $x[n, f_{l,1}, f_{h,1}]$, and the SES of the signal filtered around the band with fault information $x[n, f_{l,2}, f_{h,2}]$ are superimposed on the same plot and presented in separate plots as well. Please take note of the different y-axis scaling.

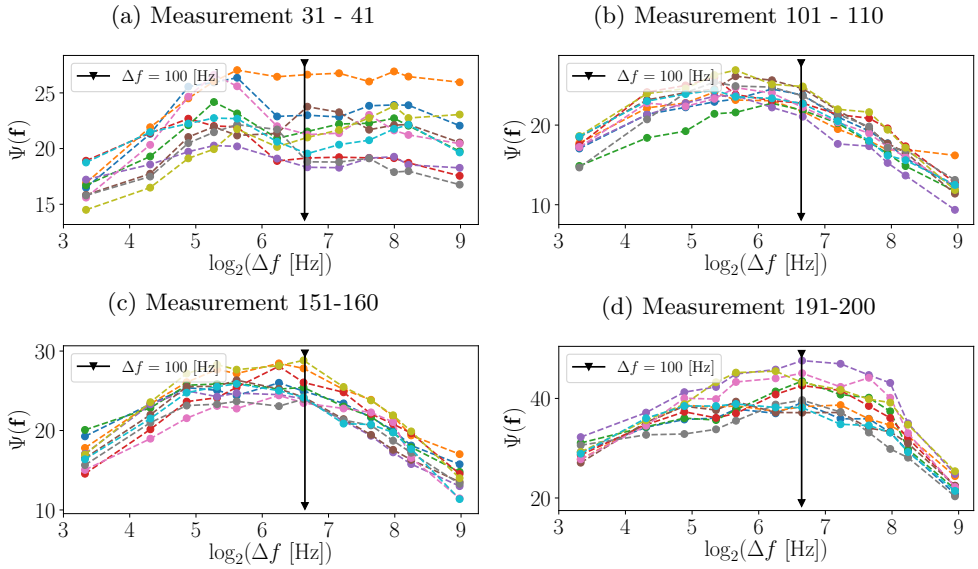

Figure C.29: The maximum value of the score function $\Psi(\boldsymbol{f})$ obtained with the initialisation procedure is shown for different bandwidths Δf and measurement numbers. The gear was missing a tooth in the measurements between 191 and 200.

Appendix C. Sensitivity analysis

The initialisation procedure discussed in Section 2.2 requires the selection of the bandwidth of the filters, which is denoted in this section as Δf. The sensitivity of the outcome of the initialisation process and subsequent optimisation process to the initial bandwidth Δf are investigated in this section. In the initialisation process, the centre frequency of the filter f_c is determined by maximising the objective function. If none of the constraints is violated the objective function is equal to the score function $\Psi(\boldsymbol{f})$ and therefore the maximisation of the objective function is equivalent to the maximisation of the score function in the feasible region.

In Figure C.29, the maximum score function $\Psi(\boldsymbol{f})$ obtained with the initialisation process is presented for different measurements and different bandwidths Δf. The bandwidth of 100 Hz, which was used for all investigations, is superimposed on the figures as well. It is clear from the results that generally the score function $\Psi(\boldsymbol{f})$ is dependent on the bandwidth as well as the measurement under consideration. The bandwidth of 100 Hz performs generally well for the considered cases.

Ultimately, it is important to determine how the bandwidth used in the initialisation procedure influences the results obtained after the optimisation process. Therefore, the outcome of the proposed procedure (i.e. the initialisation procedure and optimisation procedure) was investigated for different initial bandwidths for each measurement in the dataset. The final score of the different measurements are presented in Figure C.30. Figure C.30(a), illustrates the variation between the different window lengths and C.30(b) shows the best results that were obtained. As the damage becomes more severe (e.g. measurement 190 onwards), then the different bandwidths perform very similarly as shown in Figure C.30(a).

(a) All window lengths

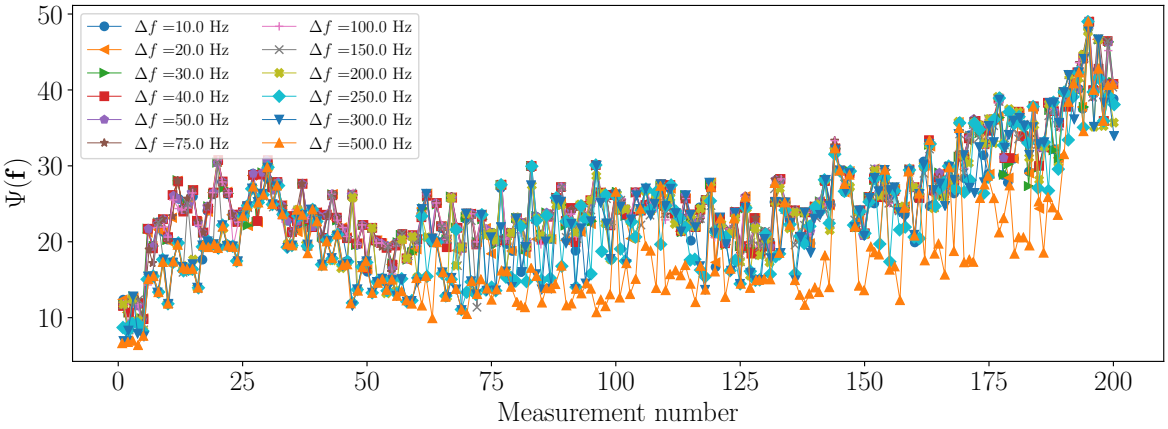

(b) Best performing window lengths

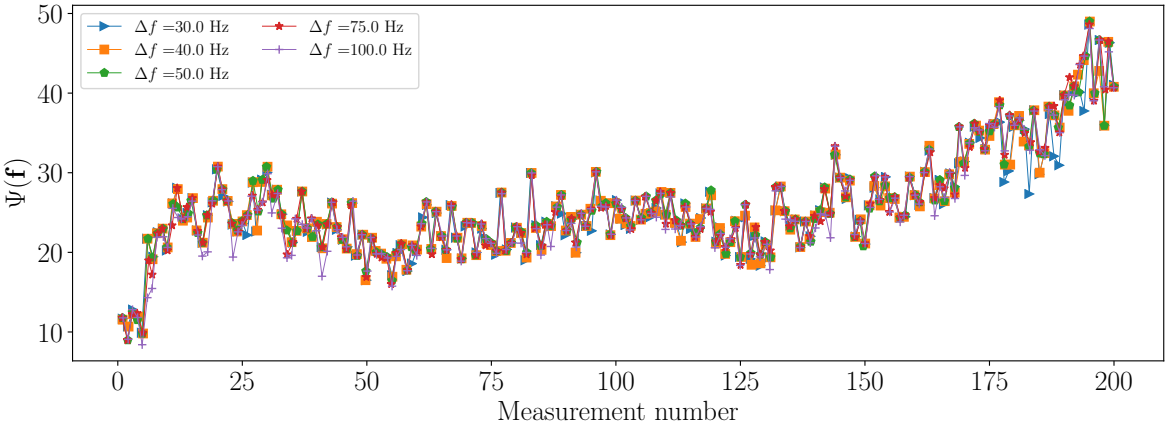

Figure C.30: The final score function, obtained after the optimisation process, is presented as a function of measurement number for different window lengths. C.30(a) shows all the considered cases and C.30(b) shows the best performing cases.

If the bandwidth is too large (e.g. larger than 200 Hz) or too small (e.g. smaller than 20 Hz), then the performance of the method is adversely affected. A large bandwidth results in the signal-to-noise ratio of the component-of-interest to decrease, which could make it difficult to detect and is detrimental to the performance of the method. A bandwidth that is too small could result in the exclusion of the important fault information, which would also impede detection.

We would, therefore, propose from this that a bandwidth that includes at least three to five harmonics should be used.

References

[1] Y. Lin, L. Tu, H. Liu, W. Li, Fault analysis of wind turbines in China, Renewable and Sustainable Energy Reviews 55 (2016) 482–490.

[2] J. Igba, K. Alemzadeh, C. Durugbo, E. T. Eiriksson, Analysing rms and peak values of vibration signals for condition monitoring of wind turbine gearboxes, Renewable Energy 91 (2016) 90–106.

[3] H. D. M. de Azevedo, A. M. Araújo, N. Bouchonneau, A review of wind turbine bearing condition monitoring: State of the art and challenges, Renewable and Sustainable Energy Reviews 56 (2016) 368–379.

[4] A. Glowacz, Recognition of acoustic signals of commutator motors, Applied Sciences 8 (12) (2018) 2630.

[5] W. Lu, W. Jiang, G. Yuan, L. Yan, A gearbox fault diagnosis scheme based on near-field acoustic holography and spatial distribution features of sound field, Journal of Sound and Vibration 332 (10) (2013) 2593–2610.

[6] F. Elasha, M. Greaves, D. Mba, D. Fang, A comparative study of the effectiveness of vibration and acoustic emission in diagnosing a defective bearing in a planetry gearbox, Applied Acoustics 115 (2017) 181–195.

[7] Y. Qu, D. He, J. Yoon, B. Van Hecke, E. Bechhoefer, J. Zhu, Gearbox tooth cut fault diagnostics using acoustic emission and vibration sensors - a comparative study, Sensors 14 (1) (2014) 1372–1393.

[8] S. H. Kia, H. Henao, G.-A. Capolino, Gear tooth surface damage fault detection using induction machine stator current space vector analysis, IEEE Transactions on industrial Electronics 62 (3) (2014) 1866–1878.

[9] M. Soualhi, K. T. Nguyen, A. Soualhi, K. Medjaher, K. E. Hemsas, Health monitoring of bearing and gear faults by using a new health indicator extracted from current signals, Measurement 141 (2019) 37–51.

[10] X. Zeng, M. Yang, Y. Bo, Gearbox oil temperature anomaly detection for wind turbine based on sparse bayesian probability estimation, International Journal of Electrical Power & Energy Systems 123 (2020) 106233.

[11] A. Grzesiek, R. Zimroz, P. Sliwinski, N. Gomolla, A. Wyłomanska, Long term belt conveyor gearbox temperature data analysis-statistical tests for anomaly detection, Measurement (2020) 108124.

[12] A. Jablonski, Z. Dworakowski, K. Dziedziech, F. Chaari, Vibration-based diagnostics of epicyclic gearboxes–from classical to soft-computing methods, Measurement 147 (2019) 106811.

[13] S. Schmidt, P. S. Heyns, Normalisation of the amplitude modulation caused by time-varying operating conditions for condition monitoring, Measurement 149 (2020) 106964.

[14] S. Kass, A. Raad, J. Antoni, Self-running bearing diagnosis based on scalar indicator using fast order frequency spectral coherence, Measurement 138 (2019) 467–484.

[15] G. Żak, M. Teuerle, A. Wyłomańska, R. Zimroz, Measures of dependence for-stable distributed processes and its application to diagnostics of local damage in presence of impulsive noise, Shock and Vibration 2017.

[16] J. Hebda-Sobkowicz, R. Zimroz, A. Wyłomańska, Selection of the informative frequency band in a bearing fault diagnosis in the presence of non-gaussian noisecomparison of recently developed methods, Applied Sciences 10 (8) (2020) 2657.

[17] D. Abboud, J. Antoni, Order-frequency analysis of machine signals, Mechanical Systems and Signal Processing 87 (2017) 229–258.

[18] S. Schmidt, P. S. Heyns, K. C. Gryllias, A pre-processing methodology to enhance novel information for rotating machine diagnostics, Mechanical Systems and Signal Processing 124 (2019) 541–561.

[19] T. Barszcz, R. B. Randall, Application of spectral kurtosis for detection of a tooth crack in the planetary gear of a wind turbine, Mechanical Systems and Signal Processing 23 (4) (2009) 1352–1365.

[20] J. Antoni, R. B. Randall, The spectral kurtosis: Application to the vibratory surveillance and diagnostics of rotating machines, Mechanical Systems and Signal Processing 20 (2) (2006) 308–331.

[21] J. Antoni, Fast computation of the kurtogram for the detection of transient faults, Mechanical Systems and Signal Processing 21 (1) (2007) 108–124.

[22] J. Antoni, The infogram: Entropic evidence of the signature of repetitive transients, Mechanical Systems and Signal Processing 74 (2016) 73–94.

[23] T. Barszcz, A. JabŁoński, A novel method for the optimal band selection for vibration signal demodulation and comparison with the kurtogram, Mechanical Systems and Signal Processing 25 (1) (2011) 431–451.

[24] Y. Lei, J. Lin, Z. He, Y. Zi, Application of an improved kurtogram method for fault diagnosis of rolling element bearings, Mechanical Systems and Signal Processing 25 (5) (2011) 1738–1749.

[25] W. A. Smith, Z. Fan, Z. Peng, H. Li, R. B. Randall, Optimised spectral kurtosis for bearing diagnostics under electromagnetic interference, Mechanical Systems and Signal Processing 75 (2016) 371–394.

[26] X. Xu, M. Zhao, J. Lin, Y. Lei, Envelope harmonic-to-noise ratio for periodic impulses detection and its application to bearing diagnosis, Measurement 91 (2016) 385–397.

[27] W. A. Smith, P. Borghesani, Q. Ni, K. Wang, Z. Peng, Optimal demodulation-band selection for envelope-based diagnostics: A comparative study of traditional and novel tools, Mechanical Systems and Signal Processing 134 (2019) 106303.

[28] A. Mauricio, W. A. Smith, R. B. Randall, J. Antoni, K. Gryllias, Improved envelope spectrum via feature optimisation-gram (iesfogram): A novel tool for rolling element bearing diagnostics under non-stationary operating conditions, Mechanical Systems and Signal Processing 144 (2020) 106891.

[29] S. Schmidt, A. Mauricio, P. S. Heyns, K. C. Gryllias, A methodology for identifying information rich frequency bands for diagnostics of mechanical components-of-interest under time-varying operating conditions, Mechanical Systems and Signal Processing 142 (2020) 106739.

[30] Q. Ni, K. Wang, J. Zheng, Rolling element bearings fault diagnosis based on a novel optimal frequency band selection scheme, IEEE Access 7 (2019) 80748–80766.

[31] T. Wang, Q. Han, F. Chu, Z. Feng, A new skrgram based demodulation technique for planet bearing fault detection, Journal of Sound and Vibration 385 (2016) 330–349.

[32] Z. Liu, Y. Jin, M. J. Zuo, D. Peng, Accugram: A novel approach based on classification to frequency band selection for rotating machinery fault diagnosis, ISA transactions 95 (2019) 346–357.

[33] Y. Zhang, R. B. Randall, Rolling element bearing fault diagnosis based on the combination of genetic algorithms and fast kurtogram, Mechanical Systems and Signal Processing 23 (5) (2009) 1509–1517.

[34] L. Wang, Y. Shao, Z. Cao, Optimal demodulation subband selection for sun gear crack fault diagnosis in planetary gearbox, Measurement 125 (2018) 554–563.

[35] M. Buzzoni, J. Antoni, G. d'Elia, Blind deconvolution based on cyclostationarity maximization and its application to fault identification, Journal of Sound and Vibration 432 (2018) 569–601.

[36] J. S. Arora, Introduction to optimum design, Elsevier/Academic Press, 2004.

[37] The MathWorks, Inc., Optimization Toolbox, Natick, Massachusetts, United State (2020).
URL `https://www.mathworks.com/help/optim/`

[38] P. Virtanen, R. Gommers, T. E. Oliphant, M. Haberland, T. Reddy, D. Cournapeau, E. Burovski, P. Peterson, W. Weckesser, J. Bright, S. J. van der Walt, M. Brett, J. Wilson, K. Jarrod Millman, N. Mayorov, A. R. J. Nelson, E. Jones, R. Kern, E. Larson, C. Carey, İ. Polat, Y. Feng, E. W.

Moore, J. Vand erPlas, D. Laxalde, J. Perktold, R. Cimrman, I. Henriksen, E. A. Quintero, C. R. Harris, A. M. Archibald, A. H. Ribeiro, F. Pedregosa, P. van Mulbregt, S. . . Contributors, SciPy 1.0: Fundamental Algorithms for Scientific Computing in Python, Nature Methods 17 (2020) 261–272. doi:https://doi.org/10.1038/s41592-019-0686-2.

[39] K. Fyfe, E. Munck, Analysis of computed order tracking, Mechanical Systems and Signal Processing 11 (2) (1997) 187–205.

[40] B. Hou, Y. Wang, B. Tang, Y. Qin, Y. Chen, Y. Chen, A tacholess order tracking method for wind turbine planetary gearbox fault detection, Measurement 138 (2019) 266–277.

[41] S. Lu, R. Yan, Y. Liu, Q. Wang, Tacholess speed estimation in order tracking: A review with application to rotating machine fault diagnosis, IEEE Transactions on Instrumentation and Measurement 68 (7) (2019) 2315–2332.

[42] D. Abboud, J. Antoni, M. Eltabach, S. Sieg-Zieba, Angle time cyclostationarity for the analysis of rolling element bearing vibrations, Measurement 75 (2015) 29–39.

[43] N. Pham, A. Malinowski, T. Bartczak, Comparative study of derivative free optimization algorithms, IEEE Transactions on Industrial Informatics 7 (4) (2011) 592–600.

[44] S. Walton, O. Hassan, K. Morgan, M. Brown, Modified cuckoo search: a new gradient free optimisation algorithm, Chaos, Solitons & Fractals 44 (9) (2011) 710–718.

[45] A. P. Engelbrecht, Computational Intelligence: An Introduction, 2nd Edition, Wiley Publishing, 2007.

[46] W. Deng, J. Xu, H. Zhao, An improved ant colony optimization algorithm based on hybrid strategies for scheduling problem, IEEE access 7 (2019) 20281–20292.

[47] F. Gao, L. Han, Implementing the nelder-mead simplex algorithm with adaptive parameters, Computational Optimization and Applications 51 (1) (2012) 259–277.

[48] K. Gryllias, S. Moschini, J. Antoni, Application of cyclo-nonstationary indicators for bearing monitoring under varying operating conditions, Journal of Engineering for Gas Turbines and Power 140 (1).